CELL ADHESION ON NANOMATER SCALE FIBRONECTIN PATTERNS: A COMPARISION OF BREAST CANCER CELLS AND NORMAL BREAST EPITHELIAL CELLS

A Thesis Submitted to

the Graduate School of Engineering and Sciences of

İzmir Institute of Technology

in Partial Fulfillment of the Requirements for the Degree of

MASTER OF SCIENCE

in Molecular Biology and Genetics

by

Utku HORZUM

December 2014

İZMİR

We approve the thesis of **Utku HORZUM**

Examining Committee Members:

_____

Assoc. Prof. Dr. Devrim PESEN OKVUR
Department of Molecular Biology and Genetics,
İzmir Institute of Technology

_____

Assist. Prof. Dr. Gülistan MEŞE ÖZÇİVİCİ
Department of Molecular Biology and Genetics,
İzmir Institute of Technology

_____

Assist. Prof. Dr. Onursal ÖNEN
Department of Mechanical Engineering,
İzmir Institute of Technology

18 December 2014

_____

Assoc. Prof. Dr. Devrim PESEN OKVUR
Supervisor, Department of Molecular Biology and Genetics,
İzmir Institute of Technology

_____

Prof. Dr. Ahmet KOÇ
Head of the Department of Molecular Biology and Genetics

_____

Prof. Dr. Bilge KARAÇALI
Dean of the Graduate School of Engineering and Sciences

ACKNOWLEDGEMENTS

First of all, the author wishes to express his gratitude to his supervisor Assoc. Prof. Dr. Devrim PESEN-OKVUR for her valuable guidance, continual support and supervision throughout this study.

The author would like to thank his colleague Berrin ÖZDİL for her support and help.

The author would also like to extend his thanks to the members of the Controlled *in vitro* Microenvironments laboratory at İzmir Institute of Technology for their team spirit.

Finally, the author would like to give his special thanks to his family for their support and encouragement during his education.

ABSTRACT

CELL ADHESION ON NANOMETER SCALE FIBRONECTIN PATTERNS: A COMPARISION OF BREAST CANCER CELLS AND NORMAL BREAST EPITHELIAL CELLS

Cell adhesion to extracellular matrix is an important process for both health and disease states. Surface protein patterns are topographically flat, and do not introduce other chemical, topographical or rigidity related functionality and, more importantly, that mimic the organization of the *in vivo* extracellular matrix are desirable. Previous work showed that vinculin and cytoskeletal organization are modulated by the size and shape of surface nanopatterns. However, a comparative and quantitative analysis on normal and cancerous cell morphology and focal adhesions as a function of micrometer scale spacings of protein nanopatterns was absent. Here, electron beam lithography was used to pattern fibronectin (FN) nanodots with micrometer scale spacings on a K-casein background (single active) on indium tin oxide (ITO) coated glass which, unlike silicon, is transparent and thus suitable for many light microscopy techniques. Exposure times were significantly reduced using the line exposure mode with micrometer scale step sizes. Micrometer scale spacings of 2, 4, 8 microns and gradients between FN nanodots modulated cell adhesion for both breast cancer and normal mammary epithelial cells, through modification of cell area, cell symmetry, actin organization, focal adhesion number, size and circularity under both static and flow conditions. Overall, cell behavior was shown to shift at the apparent threshold of 4 μm spacing. Results showed that there were significant differences in terms of cell adhesion between breast cancer and normal mammary epithelial cells: Breast cancer cells exhibited a more dynamic and flexible adhesion profile than normal mammary epithelial cells.

ÖZET

NANOMETRE ÖLÇEĞİNDE FİBRONEKTİN DESENLERİ ÜZERİNDE HÜCRE YAPIŞMASI: MEME KANSERİ HÜCRELERİ VE NORMAL MEME EPİTEL HÜCRELERİNİN KARŞILAŞTIRILMASI

Hücrelerarası maddeye hücre yapışması hem sağlık hem de hastalık durumları için önemli bir süreçtir. Topografik olarak düz ve başka kimyasal, topografik ya da sertlik ile ilgili işlevsellik getirmeyen ve daha önemlisi canlıdaki hücrelerarası madde düzenlenmesini taklitleyen yüzey protein desenleri arzu edilmektedir. Daha önceki çalışmalar göstermiştir ki vinkülin ve hücre iskeletinin düzenlemesi yüzey nanodesenlerinin büyüklüğü ve şekli ile değişmektedir. Fakat, protein nanodesenlerinin mikrometre ölçeğindeki aralıklarına bağlı olarak normal ve kanserli hücrelerin morfolojileri ve odaksal yapışmalarının karşılaştırmalı sayısal analizi eksiktir. Burada, elektron demeti litografisi kullanılarak silikondan farklı olarak şeffaf ve böylece birçok mikroskop tekniğine uygun olan indiyum kalay oksit (İTO) üzerinde K-kazein arka planında (tek aktif) mikrometre ölçeğinde aralıklarla fibronektin (FN) nanonoktaları desenlenmiştir. Yazım zamanları mikrometre ölçeğinde adım büyüklükleri ile çizgi yazım modu kullanılarak önemli ölçüde kısaltılmıştır. FN nanonoktalarının mikrometre ölçeğinde 2, 4, 8 mikron ve değişken aralıkları hem meme kanseri hücreleri hem de normal meme epitel hücrelerinde hücre yapışmasını hücre alanı, hücre simetrisi, aktin düzenlenmesi, odaksal yapışma sayısı, alanı ve daireselliği ile hem durgun hem de akış koşullarında değiştirmiştir. Toplamda hücre davranışının görünen eşik değeri olarak 4 mikron aralıkta değiştiği gösterilmiştir. Sonuçlar gösterdi ki hücre yapışması bağlamında meme kanseri hücreleri ile normal meme epitel hücreleri arasında belirgin farklar bulunmaktadır: Meme kanseri hücreleri normal meme epitel hücrelerinden daha dinamik ve esnek bir yapışma profili sergilemişlerdir.

To Berkin ELVAN...

TABLE OF CONTENTS

LIST OF FIGURES

LIST OF ABBREVIATIONS

EBL	Electron Beam Lithography
ITO	Indium Tin Oxide
FN	Fibronectin
Kcas	K-casein
FA	Focal Adhesion
ECM	Extracellular Matrix
DMSO	Dimethylsulfoxide
APTES	3-Aminopropyl Triethoxy-silane
PBS	Phosphate Buffered Saline
UB	Universal Buffer
DMEM	Dulbecco's Modified Eagle's Medium
EGF	Epidermal Growth Factor
L-15	Leibovitz's 15
BSA	Bovine Serum Albumine

CHAPTER 1

INTRODUCTION

1.1. Significance of Focal Adhesion in Cell Biology

Focal adhesions are protein compositions involved in mechanical and chemical interactions of the cells with their environments. These structures play a key role in metastasis, angiogenesis, tumorigenesis, embryonic development, tissue homeostasis, atherosclerosis and wound healing. Focal adhesions provide cell adhesion which is an important dynamic process to regulate cell behaviour and fate for both normal and cancer cells (Berginski, Vitriol, Hahn, & Gomez, 2011; Berrier & Yamada, 2007; Zaidel-Bar, Cohen, Addadi, & Geiger, 2004). Spatial organisation and mechanical properties of adhering cells are regulated by integration of cells and their extracellular environments via focal adhesions. The properties of extracellular environment, biological content, topography and mechanics, are determinative as leading to diverse behaviors (Parsons, Horwitz, & Schwartz, 2010; Wozniak, Modzelewska, Kwong, & Keely, 2004).

Focal adhesions are between cell and extracellular matrix vary between 10 nanometer to 10 micrometer in size. Focal adhesions are composed of more than hundred proteins mainly based on fibronectin in extracellular matrix, integrin as transmembrane protein and vinculin as intracellular protein (Zaidel-Bar et al., 2004; Zamir & Geiger, 2001). Focal adhesions mainly participate in regulation of cell behavior via protein interactions; they are both mechanic sensors and adhesion structures. They regulate cell adhesion, migration and differentiation (Schwarz, Erdmann, & Bischofs, 2006; Zhao & Guan, 2009).

1.2. Extracellular Matrix

Extracellular matrix is a complex and dynamic network of macromolecules. This network coats outer surface of the cells and forms a biological environment with different physical and biochemical properties for the cells in a tissue. Physical properties like rigidity, porosity, topography and insolubility of extracellular matrix provide the

occurence of various anchorage-related biological functions like cell migration, division and cell/tissue polarization. Biochemical properties of the extracellular matrix initiate some signal pathways. Various binding sites for some cell surface receptors are found on the protein component of matrix and also non-canonical presentation of growth factors is provided by matrix. Extracellular matrix is tissue-specific because of the variable macromolecule composition and organization, moreover it is dynamic because of the regulation of production, degradation and remodeling of the extracellular matrix composition (Gattazzo, Urciuolo, & Bonaldo, 2014). Extracellular matrix properties are altered pathologically and this can be the cause or result of many diseases. In cancer patients it is seen that extracellular matrix production is excessive and has abnormal architecture in comparison to normal conditions. For instance, it is known that extracellular matrix from the breast cancer patients contains higher levels of collagen and proteoglycan than the healthy controls (Gill & West, 2013). Extracellular matrix is composed of collagen and elastin intensively, in addition to these, proteins of extracellular matrix fibronectin, laminin and other proteoglycans and glycoproteins are included in composition. Fibronectin and laminin are the most abundant glycoproteins in the extracellular matrix, which are associated with collagen, heparin and other fibronectin or laminin proteins. Modular characters of laminin and fibronectin are determinative on both branched protein network formation and assembly of collagen in the extracellular matrix. As well as intrinsic properties of these matrix components, cells also recognize some amino acid sequences of proteins like collagen, fibronectin and laminin by integrin receptors and this provide an additional cell control to organize extracellular matrix (Aumailley & Smyth, 1998; Muiznieks & Keeley, 2013).

1.3. Mimicking of Extracellular Matrix

The architecture and composition of extracellular matrix provide physical and biochemical cues, which direct cell behavior. Major sensors of the cells are integrins with their constituent role of forming focal adhesions in adhesive structures of cells. Extracellular matrix adhesive features has been widely investigated on the uniformly coated sheet-like (2D) surfaces with large-scale patterning approaches. However, cells produce extracellular matrix structures ranging from nanometers up to micrometers with a high complexity which are adhesive patches and non-adhesive spacings (Wolf et al.,

2014; Kim, Provenzano, Smith, & Levchenko, 2012; Provenzano, Eliceiri, & Keely, 2009; Soucy & Romer, 2009; Zoumi, Yeh, & Tromberg, 2002).

There have been important cell adhesion studies depending on biomimetric surfaces fabricated by mimicking of extracellular matrix (Agheli, Malmström, Larsson, Textor, & Sutherland, 2006; Alsberg et al., 2006; Biggs, Richards, & Dalby, 2010; Cavalcanti-Adam et al., 2007; Chen, 1997; Elineni & Gallant, 2011; Gingras et al., 2009; Li, Shi, Deng, Lo, & Liu, 2012; Lutz, Pataky, Gadhari, Marelli, & Brugger, 2011; Malmstr et al., 2011; Oliva, James, Kingman, Craighead, & Banker, 2003; Park, Kim & Kim, 2012; Pesen & Haviland, 2009). Now, it is well appreciated that cell adhesion over the fabricated surfaces can be strongly affected both by rigidity and the architecture of biomimetric surfaces. So far, these studies have answered the questions about the cell-matrix interaction at micrometer scale; but the crucial event in the cell attachment is the recognition of extracellular matrix components via integrins and examination of these interactions needs to fabrication of extracellular matrix-mimicking substrate over the micrometer scale. Nanometer scale resolution provides well-controlled nanofabricated biomimetric surfaces to examine the effects of extracellular matrix properties on the cells. Despite the advences in nanofabrication technology, micropatterned surfaces form large areas with uniform adhesiveness and these surfaces are highly combined for topological, biochemical and rigidity signals (Alsberg et al., 2006; Cavalcanti-Adam et al., 2007; Lussi et al., 2004, 2005; Jinseok Park et al., 2012). These three signals are important for examination of cell behavior and ideally should be examined individually, in fact analysis of the effects of one of these signals prevent the interpretation of a combined signal like a type of sensing. So, there are important studies done with protein surface patterning, but in these studies, surfaces contains both biochemical and topological signals simultaneously owing to the method of fabrication. Usage of multiple oxide layers inevitably result with formation of topography variations together with biochemical variations. In this case, cells respond to the fabricated surfaces because of topographical signal (high versus low regions on the surface) and biochemical signal (protein versus polymer), which can be confusing (Lussi et al., 2004, 2005). Patterning is also done with gold particles bounded polymers of various lengths, while controlling of distance between proteins is provided impeccably, this method does not supply fabrication of patterns with varying spaces and gold particles on the surface cause additional signals as well (Cavalcanti-Adam et al., 2007). In this area, electron beam lithography (EBL) method uses focused (~ 2 nm in diameter) electron beams in nanoscale with high resolution.

Electron beam lithography is a direct writing method; does not need light mask and can process from nanometer to centimeter spaced patterns. Electron beam lithography method has the capacity to be used in cell biology research. Up to now, protein patterning has been successful and these surfaces have been tested for functionality at cellular level (Alonso, Ondarçuhu, & Bittner, 2013; Hoa et al., 2008; Palankar, Medvedev, Rong, & Delcea, 2013; Pesen, Erlandsson, Ulfendahl, & Haviland, 2007; Pesen & Haviland, 2009; Pesen, Heinz, Werbin, Hoh, & Haviland, 2007; Ron, Lee, Amar, Ghassemi, & Hone, 2011; Rundqvist et al., 2007). A study revealed that this patterning method only supplies biochemical signals and patterned surfaces do not have rigidity signals. Another advantage is incorruption of flatness of surface in which thickness of only 2 nm can be ignored (Pesen, Erlandsson, et al., 2007). Electron beam lithography comes into prominence with possibility of patterning two protein simultaneously owing to direct usage of one of the protein as EBL resist (Pesen & Haviland, 2009). Preliminary studies show that protein on the surface (for instance fibronectin) is inactivated with the focused electron beams (Rundqvist et al., 2007).It has been achieved that the direct inactivation of first protein layer or resist by electron irradiation. Binding of a second species of protein to these electron beam exposed areas provide biofunctional surfaces at the cellular level. In this way, the protein of interests can be selected to form defined architecture with only biochemical signals. In one of the case studies, K-casein coated surface patterned with dots and ring motifs with electron beam lithography and then coated with fibronectin. This biofunctional surfaces have been used for the analysis of vinculin and actin cytoskeleton organization of the cells on this differently shaped fibronectin nanopatterns (Pesen & Haviland, 2009; Pesen, Heinz, et al., 2007). While patterning with electron beam lithography has many advantages over other known methods, usage of silicon substrate complicate many downstream light microscopy applications because of its low transparency. Instead of silicon, transparent indium tin oxide coated glass remove the limitations about light microscopy applications for especially cell biology studies (Horzum, Ozdil, & Pesen-Okvur, 2014a).

1.4. Mechanism and Components of Focal Adhesion

Focal adhesions initially observed by Ambrose (1961) as the structures between cells and solid surface using the surface contact light microscope and later their closest distance to the surface was reported as approximately 10 nm by Curtis (1964) using interference reflection microscope. From the point of morphological perspective, focal adhesions divide into two groups which are ‘dot’ and ‘dash’ variants. Small initial contacts represent ‘dot’ variants with dimensions of 0.2 – 0.5 μm. These predominant contacts consist of transmembrane and some linker proteins but there is not any prominent association with actin cytoskeleton. As distinct from ‘dot’ variants, elongated mature contacts or ‘dash’ variants are associated with actin cytoskeleton together with accumulation of transmembrane and some linker proteins. Dimensions of dash contacts are 2 – 10 μm in length and 0,5 μm in width. Furthermore, the localization of these two variants reflect another difference that initial contacts or dot variants are born at the leading edge of protruding lamellipodia. Most of them are disassembled in seconds dynamically, remaning initial contacts mature and become longer-lived structures under a tight regulation by structural and signaling molecules. These structures are observed at the end of the lamellipodia and at the beginning of lamella wherein some of them continue to grow by recruitment of additional structural molecules and non-growing adhesion undergoes disintegration and disappear. Growing focal adhesions get into a higher maturation step with the association of actin bundles and accumulation of additional structural molecules occur to form an elongated or dash variant. These dash variants have a minimum lifetime of 20 minutes and they usually localize at the center of lamella. Dash or mature focal adhesions bridge extracellular portion of the cell to the intracellular actin cytoskeleton providing force transmission (Berginski et al., 2011; Hoffman, Grashoff, & Schwartz, 2011; Owen, Meredith, ap Gwynn, & Richards, 2005).

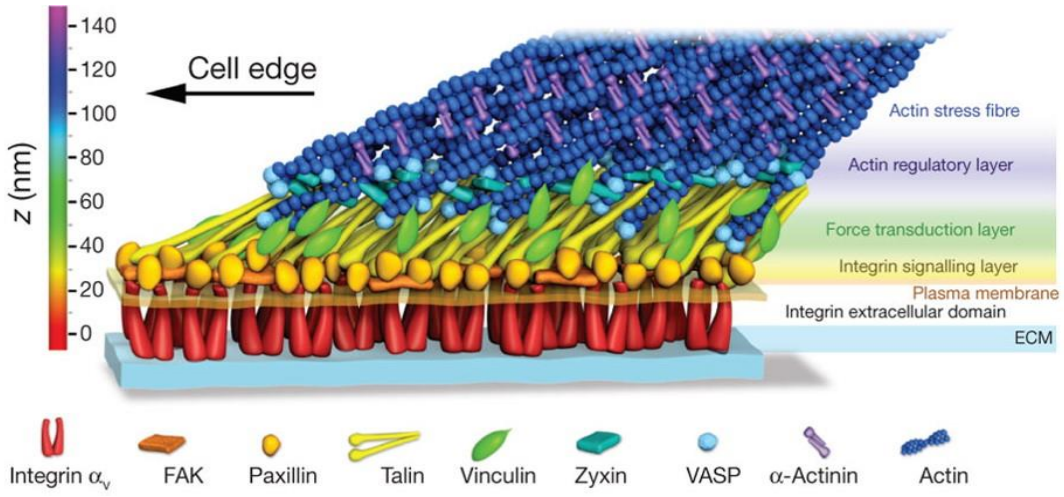

Figure 1.1. Schematic representation of focal adhesions. Experimentally determined protein positions are used to model molecular architecture of focal adhesion (Source: Kanchanawong et al., 2010).

Focal adhesions are integrin-based biological structures. Transmembrane integrin receptors recognize and bind to some specific sequences on the molecules of extracellular matrix to couple the extracellular matrix to the actin cytoskeleton by recruitment of actin binding proteins at the cytoplasmic domains of integrins. The integrin family comprises 18α and 8β subunits which generate 24 distinct identified αβ heterodimeric integrin receptors. Each receptor has overlaps for ligand protein in the repertoire of extracellular matrix (Boudreau & Jones, 1999; Ciobanasu, Faivre, & Le Clainche, 2013). When integrin receptors bind to their ligand in the extracellular matrix, integrins undergo two different biochemical changes. Firstly structural changes take place, and then phosphorylation of cytoplasmic tails occur. While structural changes strengthen the binding of integrins to their ligands, these changes also increase the potential of clustering of integrins at the cell membrane. Furthermore, phosphorylated cytoplasmic domain of integrins become available for binding some linker and regulator proteins in the cells for the regulation of adhesions (Blystone, 2004). An epitope of integrin is a section of the matrix protein's amino acid sequence, for example arginine-glycine-asparagine is a well-known amino acid sequence for binding of a group of integrin and this sequence is found on fibronectin, vitronectin and fibrinogen proteins of extracellular matrix (Owen et al., 2005). In the cell, there are approximately 150 proteins including kinases, phosphatases and structural proteins, having role for the formation of focal adhesions, additionally more than 600 proteins are responsible for the regulation of these dynamic structures (Le Dévédec et al., 2010). Maturation of a focal adhesion depends on the suitability for an

effective force transmission. Interaction of integrins with actin cytoskeleton is conserved and enhanced by some stabilizer proteins such as vinculin and talin (Figure 1.1) (Harjanto & Zaman, 2010). Talin binds actin filaments to the cytoplasmic tails of integrins and by this function it exhibits high importance for establishment and consolidation of mature focal adhesions. α-actinin crosslinks actin filaments and interacts with zyxin and vinculin. Zyxin facilitates the assembly of other functional molecules at the site of integrin-actin interactions. Moreover, it has been reported that phosphotidyl inositol-4-5 biphosphate (PIP2) interact with this region. From the family of non-receptor protein tyrosine kinase, focal adhesion kinase (FAK) are also found in this interaction region and FAK gains its enzymatic activity as a result of biochemical changes on integrins being with ligand engagement. Active FAK involved in signal cascades regulating cell spreading, migration and generation of adhesion-dependent anti-apoptotic signals. Paxilin and tensin are principally localized at the actin-integrin interaction region as the downstream components of FAK signalling. Vinculin is a specific linker protein involved in multiple binding interactions at membrane-actin attachment sites. Vinculin provides actin attachment to the integrins and further stabilizes focal adhesions by interacting partners such as talin, α-actinin, paxillin, vasodilator-stimulated phosphoprotein, Arp2/3 and other acidic phospholipids. Vinculin changes its conformation from curled state to linear state by induction of PIP2 and this conformational change makes protein-binding sites available for direct interactions during the maturation of focal adhesions. Identification of a focal adhesion is possible by labeling any protein in this complex, although each component or protein has a specific feature, labeling of lots of these components is inconvenient. For example, integrins have a major role in the focal adhesions but their heterodimeric structures known 24 distinct αβ integrin receptors could not be labeled easily and this process is quite impractical. There are three candidates to identify focal adhesion complex effectively, these candidates are α-actinin, talin and vinculin. Immunolabeling of α-actinin is possible but this protein is also observed in other locations of actin filaments at the outside of actin-membrane interaction sites. Talin and vinculin are convenient for the immunolabeling of focal adhesion complexes. Vinculin has some additional advantages when compared with talin that first of all its head-to-tail structure makes it available for binding interactions of more proteins and secondly vinculin has commercial monoclonal antibodies from several species. These factors provide possibility to obtain a good level of signal and have applications on many cell types

(Ciobanasu et al., 2013; Hoffman et al., 2011; Hytönen & Wehrle-Haller, 2014; Owen et al., 2005; Thievessen et al., 2013).

1.5. Actin Polimerization and Force Transmission

Actin organization is preliminarily responsible for cell shape and intracellular molecular transport to process various cellular processes such as migration, morphogenesis, endocytic and exocytic pathways. The most important role of actin organization is assurance of force transmission via active polymerization and depolymerization under the control of a large group of actin-binding proteins especially during cell migration (Fletcher & Mullins, 2010; Tojkander, Gateva, & Lappalainen, 2012). The observation of actin stress fibers associated with focal adhesions has supported that structure and dynamics of actin networks is essential for force transmission (Goode & Eck, 2007; Romero et al., 2004). There are at least three groups of actin stress fibers in the cells: (i) transverse arcs are curved actin filament bundles which are connected to focal adhesions through intrections with dorsal fibers along the long axis, (ii) dorsal stress fibers attach to focal adhesions at cell periphery by their distal ends and elongate towards to center regions of the cell, and (iii) ventral stress fibers attach to focal adhesions with both ends at the posterior site of the cell (Figure 1.2) (JinSeok Park, Kim, Kim, Levchenko, & Suh, 2012).

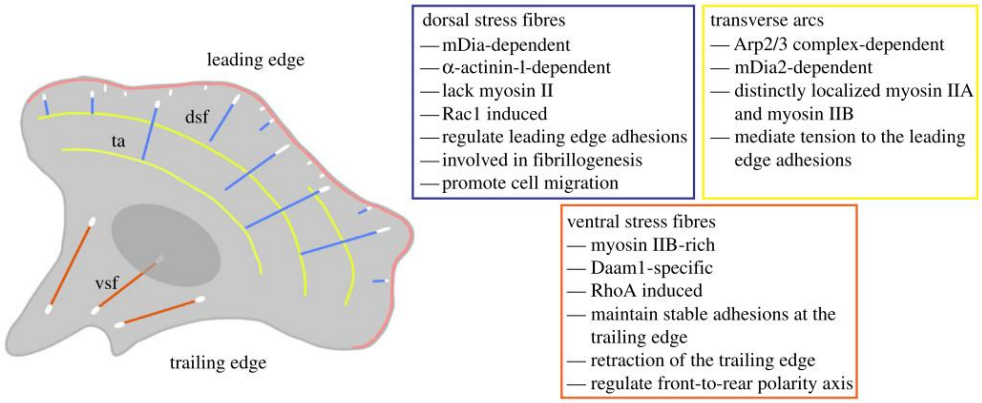

Figure 1.2. Schematic representation of the actin stress fibre subtypes. Each subtype has a color code. Branched network of actin filaments are seen as a red curved line at the leading edge (Source: Vallenius, 2013).

Actin structures are remodeled with interconnected status of polymerization and depolymerization processes. Vasodilator-stimulated phosphoprotein (VASP), Mena, and proteins of Ena-VASP family have emerged as essential factors for actin assembly or polymerization unlike vinculin and tensin proteins inhibit the actin polymerization at the actin ends. Here, vinculin shows a cap-like inhibition on the actin polymerization (Krause, Dent, Bear, Loureiro, & Gertler, 2003; Le Clainche, Dwivedi, Didry, & Carlier, 2010). Actin networks associated with focal adhesions insulate the tension of the extant force on the cell. Beside force transmission, actin polymerization provides formation of protruding edges of cell membrane during movement. Furthermore anisotropic clustering of actin filaments provides cellular polarization (Cramer, Siebert, & Mitchison, 1997).

1.6. Integrins

Integrins are transmembrane adhesion proteins expressed in only metazoa. In human, there have been 18α and 8β integrin subunits which generate 24 identified distinct αβ heterodimeric integrin receptors (Figure 1.3). Each subunit interacts with each other non-covalently. Every cell of mammals express integrins, however the expressed type and the rate of expression for a type of heterodimer is cell-dependent. For example, platelets have lots of αIIβ3 integrin receptors on their cell membrane and expression of this integrin receptor is essential for functionality of these cells that αIIβ3 integrin receptors recognize fibrinogen, von Willebrand factor and fibronectin (Gilcrease, 2007;

Hynes, 2002). In the case of epithelial cells, most integrins are β1-containing heterodimers which are laminin and collagen recognizing α1 β1, α2 β1, α3 β1, and α6 β1 integrins. In addition, expression of epithelial specific integrins including α6 β4, α5 β1, and αV β3 provides the recognition of RGD peptide motif containing proteins of extracellular matrix such as fibronectin (Gilcrease, 2007; Matlin, Haus, & Zuk, 2003). Particular extracellular regions of α and β subunits form a globular head domain that binds an extracellular protein with an acquired ligand specificity. Although intracellular part of integrins is a short tail without enzymatic activity, recruitments of other adaptor and signaling molecules to the site of integrin-matrix contact are ensured by clustering of integrin tails at the inner side of membrane. In conclusion, integrins are core proteins of cell-matrix adhesion and also signal units at the result of mutual interactions between many accumulated proteins surrounding integrin tail clusters (Danen & Yamada, 2001).

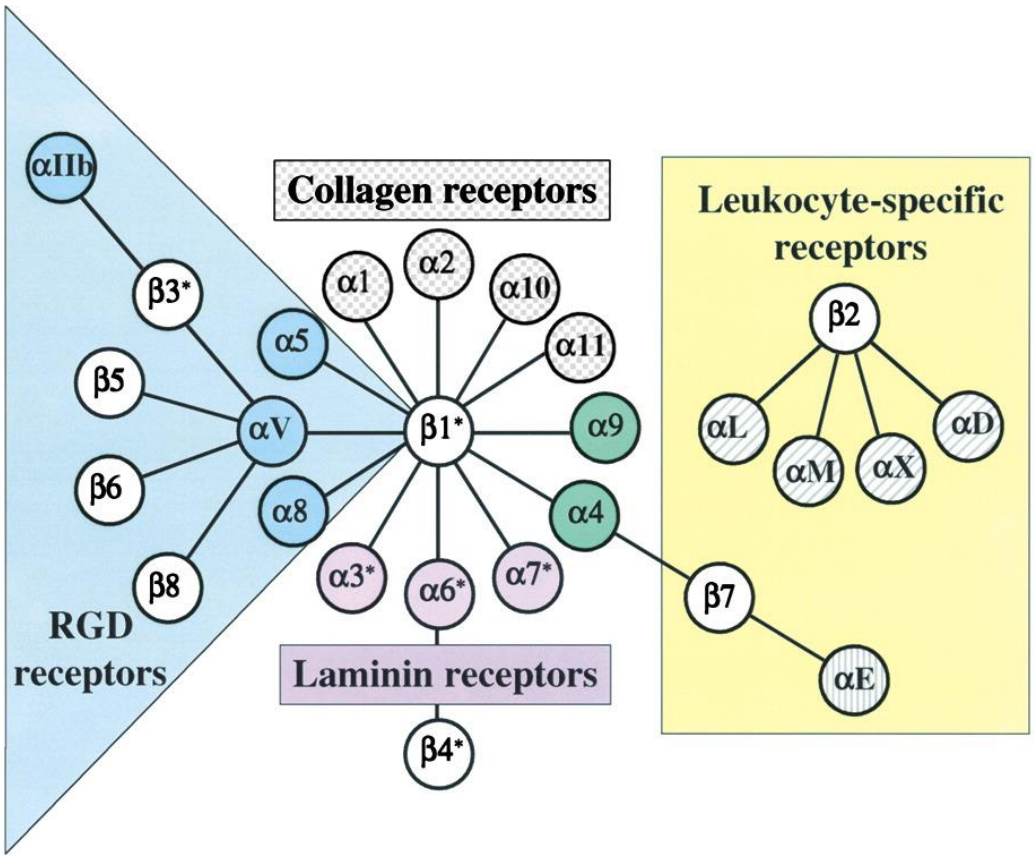

Figure 1.3. Mammalian integrin receptor family. 18α and 8β subunits which generate identified 24 distinct αβ heterodimeric integrin receptors (Source: Hynes, 2002).

Individiual cell migration classified in two categories either amoeboid and mesenchymal. Integrin-based cell adhesions have a major role for mesenchymal migration when compared it with amoeboid migration. Mesenchymal migration needs transient formation of focal adhesions together with a dynamic cytoskeletal activity. Here, it is known that more adhesive cells are slowly they migrate (Friedl & Wolf, 2010). Cancer cells can switch their migration type according to environmental cues since metastasis needs an adaptation capability to invade different environments. If invader shows amoeboid migration, cells are rounded or ellipsoid with the absence of mature focal adhesions and stress fibers except actin-rich filopodia and weak adhesive interactions. There are considerable expression differences of integrins between cancer and normal cells. Furthermore, different types of cancer have diversity for their integrin expression. αVβ3, α5β1 and αVβ6 integrins are usually upregulated in cancer cells, on the other hand, there are downregulated integrins for cancer cells such as α2β1. It is clear that variations of integrin expression results in the change of cell behaviour. When α2β1 expression level is increased in breast cancer cells, it is observed that cells weakened their proliferation

and migration characters as a result of increased anchorage dependency by α2β1(van Dijk, Göransson, & Strömblad, 2013). Beside these, polarized cells localize integrins to their membranes according to polarization requirements. Cancer cells also lose their specific integrin distributions to provide polarization. For example, α6β4 integrins are localized to the basal surface of epithelial cells, however cancer cells show approximately homogenous distribution of α6β4 integrins and interestingly these integrins become localized to the leading edge during migration (Gilcrease, 2007; Natali, Botti, & Bigottil, 1992). In consequence of expression changes, cells exhibit different invasion potentials, MDA-MB-231 cancer epithelial cells have high invasion activity with a mean invasion index of 42.1% and MCF10A normal epithelial cells are less invasive with a mean invasion index of 37.7% (Natali et al., 1992).

1.7. Flow-induced Shear Stress

Metastasis is a process with consecutive steps which are local invasion, intravasation, circulation, arrest-extravasation, proliferation and angiogenesis. If a cancer cell escape from primary tumor site and complete these metastatic steps, it can colonize to a distant location and form a secondary tumor. Here, it is known that only a small fraction of primary cancer cells have the ability to colonize a secondory site but metastasis is the major cause of cancer-related death (Beerling, Ritsma, Vrisekoop, Derksen, & van Rheenen, 2011; Chaffer & Weinberg, 2011). Tumor cells are exposed to mechanical stress at their primary site by interstitial flow or upon in circulation by blood flow. Interstitial flow can modulate metastasis and invasion by acting on tethering force of cell-matrix connections (Chang et al., 2007). Interstitial flow causes shear stress on the cells in the range of 0.007 – 0.015 dyn cm^{-2}. This is an estimated interval for tissues. When tumor cells enter to the circulation, these circulating tumor cells are exposed to the higher shear stresses, so measured intervals which are range from 0.5 to 4.0 dyn cm^{-2} in venous circulation and 4.0 to 30.0 dyn cm^{-2} in arterial circulation. Microfluidic devices are advisable to test effects of shear stress on cells. In these devices, defined shear stress values can be tested with minimum sample volumes. Shear stress is found as $\tau = 6\eta Q / wh^2$, where η is the viscosity of fluid, Q is the flow rate, w is the width of channel and h is the height of channel in microfluidic device (Gutierrez et al., 2008; Mitchell & King, 2013). It has been reported that fluid shear stress affects the cell morphology, calcium

transport, gene expression and cell adhesion of attached cells on the homogeneously protein coated surfaces (B P Helmke, Thakker, Goldman, & Davies, 2001; B. P. Helmke, Goldman, & Davies, 2000; Jang et al., 2011; Kou et al., 2011; Lawler, O'Sullivan, Long, & Kenny, 2009; Lu et al., 2004; Tzima, del Pozo, Shattil, Chien, & Schwartz, 2001; Zhu, Yago, Lou, Zarnitsyna, & McEver, 2008).

In this study, firstly we aimed to realize protein-only based surface patterning on ITO surfaces with defined geometry and organization of extracellular matrix protein, fibronectin. Secondly, we aimed to make a comparative and quantitative analysis on normal and cancerous cell morphology and focal adhesions as a funtion of micrometer scale spacings of fibronectin nanopatterns under both stationary conditions and flow-induced stress conditions.

CHAPTER 2

MATERIALS AND METHODS

2.1. Cell Culture

MDA-MB-231 and MCF10A cell lines were used. MDA-MB-231 growth medium was prepared with 450 ml of high glucose DMEM (Dulbecco's Modified Eagle's Medium-Biological Industries(01-055-1A)), 50 ml of fetal bovine serum (Biological Industries(04-001-1A)), 5 ml of penicilin-streptomycin (Biological Industries(03-031-1B)) and 5 ml of L-glutamine (Biological Industries(03-020-1B)) that all components were mixed properly and filtered before usage. MCF10A growth medium was prepared with 500 ml of DMEM/F12 (Biological Industries(01-170-1A)), 25 ml of donor horse serum (Biological Industries(04-004-1A)), 100 µl of EGF (Sigma(E96442 MG)), 250 µl of hydrocortisone (Sigma (H0888-1G)), 500 µl of insulin (Sigma(I1882-100MG)), 50 µl of choleratoxin (Sigma (C8052-1MG)), 5 ml of penicilin-streptomycin (Biological Industries(03-031-1B)) and 5 ml of L-glutamin (Biological Industries(03-020-1B)) that all components were mixed properly and filtered before usage. Starvation medium was prepared with 500 ml of Leibovitz's (1X)) L-15 (gibco by life technologies(21083-027)) and 1,725 gram bovine serum albumin (Sigma-(A9418)) that all components were mixed properly and filtered before usage. All cell culture protocols were followed in laminar flow cabinets (Thermo Scientific MSC1.2 and Nüve MN120). Cells were grown in 100 mm treated petri dishes (Corning 100 mm TC-Treated culture dish) at 37^{o} C and 5% CO_2 in incubators (Binder ve ThernoScientific 3404). Cells were observed under phase-contrast microscope (Olympus CKX41) in order to evaluate growth ratios.

2.1.1. MDA-MB-231 Cell Culture

MDA-MB-231 cells passaged every 2-3 days. MDA-MB-231 cells were convenient for experiment between passage numbers of 30 and 50. MDA-MB-231 cells were preserved in liquid nitrogen for long term storage. MDA-MB-231 cell requirements were provided by thawing of these frozen cells. For thawing, first of all, cell medium was

transferred in culture dish and placed into incubator for warming and gas balancing. Afterwards, cryovial tube including frozen cells was removed from liquid nitrogen tank (Thermo Scientific Locator JR Plus) and was hold in 37^{o} C water bath (Nüve bath nb2) until sides were thawed but center remained frozen. As well as observation of this self-frozen stage, solution was transferred into a falcon tube and completed to 10 ml with the addition of warm media dropwise to the partially frozen cells. This solution was placed in a centrifuge (Nüve bench top centrifuge NF 400R) and centrifuged at 1000 rpm and 4^{o} C for 5 minutes. Supernatant was removed with a pasteur pipette and pellet was quickly re-suspended by adding 1 ml cell medium. This resuspended cell solution was transferred into the warmed cell medium and placed in the incubator again. After one day or as soon as cells are attached, cell medium was changed in order to remove residual DMSO. Recovery of cell growth needs at least a week. When cells showed over 80% confluency two days later of last passage, they were used for next passage. For passaging, firstly cell medium transferred in culture dish and placed into incubator for warming and gase balancing. Cell culture petri dish was taken from incubator and medium was aspirated then immediately 2 ml of trypsin was added and aspirated in order to remove trypsin inhibitory factors. Cells again trypsinized with 4 ml of trypsin and petri dish was placed into incubator for obtaining of optimum enzymatic activity. After 3 minutes, most of the cells were thrown over the surface of petri dish and attachments weakened for remainings. Trypsin was inhibited by adding 1 ml medium. Solution including trypsin and medium transferred into a falcon tube. Later petri dish was washed with addition of 5 ml medium and similarly transferred into same falcon tube. Before the transfer processes, physical forces were applied to petri surface to leave weakly attached cells by pipetting of solution. This collected cell suspension in falcon tube was located in a centrifuge (Nüve bench top centrifuge NF 400R) and centrifuged at 1000 rpm and 20^{o} C for 5 minutes. Supernatant was removed with a pasteur pipette and pellet was quickly re-suspended by adding 1 ml cell medium. This resuspended cell solution was transferred into the warmed cell medium and placed into incubator again. For long term storage and conservation of cell stock, MDA-MB-231 cells were froze at early passage numbers. In the purpose of this, cells trypsinized (standard cell passage protocol) and centrifuged at 1000 rpm and 20^{o} C for 5 minutes. Cell pellet was resuspended with freezing medium which contains additional 7% dimethylsulfoxide (DMSO) in cell medium. Resuspended cells was transferred into cryovials (1 ml per vial) as aliquots. Aliquots were placed into reservoir of iso-propanol

containing freezing container and were froze overnight at -80^{o} C. Lastly, cryovials were transferred in liquid nitrogen tank for indefinite storage.

2.1.2 MCF10A Cell Culture

MCF10A cells passaged every 2-3 days. MCF10A cells were convenient for experiment between passage numbers of 10 and 30. MCF10A cells were preserved in liquid nitrogen for long term storage. MCF10A cell requirements were provided by thawing of these frozen cells. For thawing, first of all, cell medium transferred in culture dish and placed into incubator for warming and gase balancing. Afterwards, cryovial tube including frozen cells was removed from liquid nitrogen tank (Thermo Scientific Locator JR Plus) and was hold in 37^{o} C water bath (Nüve bath nb2) until sides were thawed but center remained frozen. As well as observation of this self-frozen stage, solution was transferred into a falcon tube and completed to 10 ml with addition of warm media dropwise to the partially frozen cells. This solution was located in a centrifuge (Nüve bench top centrifuge NF 400R) and centrifuged at 1000 rpm and 4^{o} C for 5 minutes. Supernatant was removed with a pasteur pipette and pellet was quickly re-suspended by adding 1 ml cell medium. This resuspended cell solution was transferred into the warmed cell medium and placed into incubator again. After one day or as soon as cells are attached, cell medium was changed in order to remove residual DMSO. Recovery of excepted cell behaviour or growth needs at least a week. When cells showed over 80% confluency two days later of last passage, they were used for next passage. For passaging, firstly cell medium transferred in culture dish and placed into incubator for warming and gase balancing. Cell culture petri dish was taken from incubator and medium was aspirated then immediately 2 ml of trypsin was added and aspirated in order to remove trypsin inhibitory factors. Cells again trypsinized with 4 ml of trypsin and petri dish was placed into incubator for obtaining of optimum enzymatic activity. After 17 minutes, most of the cells threw over the surface of petri dish and attachments weakened for remainings. Trypsin was inhibited by adding 1 ml medium. Solution including trypsin and medium transferred into a falcon tube. Later petri dish was washed with addition of 5 ml medium and similarly transferred into same falcon tube. Before the transfer processes, physical forces were applied to petri surface to leave weakly attached cells by pipetting of solution. This collected cell suspension in falcon tube was located in a centrifuge (Nüve bench top

centrifuge NF 400R) and centrifuged at 1000 rpm and 20^{o} C for 5 minutes. Supernatant was removed with a pasteur pipette and pellet was quickly re-suspended by adding 1 ml cell medium. This resuspended cell solution was transferred into the warmed cell medium and placed into incubator again. For long term storage and conservation of cell stock, MCF10A cells were froze at early passage numbers. In the purpose of this, cells trypsinized (standard cell passage protocol) and centrifuged at 1000 rpm and 20^{o} C for 5 minutes. Cell pellet was resuspended with freezing medium which contains additional 7% dimethylsulfoxide (DMSO) in cell medium. Resuspended cells was transferred into cryovials (1 ml per vial) as aliquots. Aliquots were placed into reservoir of iso-propanol containing freezing container and were froze overnight at -80^{o} C. Lastly, cryovials were transferred in liquid nitrogen tank for indefinite storage.

2.2. Chip Preparation

2.2.1. Cleaning of ITO-coated Glasses

ITO (indium tin oxide) coated glasses were purchased from TEKNOMA (İzmir, Turkey). ITO coated surface was checked by multimeter to confirm conductivity. Cleaning of glasses was provided by sequential washing steps and UV/Ozone exposure. Glasses were sonicated in acetone, iso-propanol and ultra-pure water for 2-3 minutes. Afterwards, glasses were exposed to UV/Ozone (BioForce Nanosciences, Inc., USA) for 10 minutes.

2.2.2. Protein Coating of ITO-coated Glasses

After cleaning, ITO coated surfaces of glasses were treated with 3% APTES (3-aminopropyl triethoxy-silane, in acetone) for 30 minutes at room temperature. Then, glasses rinsed with acetone and ultra-pure water, lastly glasses were left in 110^{o} C oven for 1 hour and cooled to slowly at room temperature. The APTES coated ITO glasses were incubated in 0,5% glutaraldehyde (in 1X PBS) for 15 min and rinsed with 1X PBS (phosphate buffered saline) and 1X UB (universal buffer) just before protein treatment. Finally, coated surfaces of glasses were incubated with 2 mg ml^{-1} K-casein for 24 hours at room temperature. After incubation, glasses rinsed with universal buffer and ultra-pure

water, dried with gase nitrogen and stored under vacuum in a dessicator until use. Same procedure was followed for fibronectin coating but in this case glasses were incubated with 0,05 mg ml^{-1} fibronectin for 2 hours at room temperature. After electron beam lithography, patterned ITO-glasses were backfilled with 0,05 mg ml^{-1} fibronectin for 2 hours at room temperature and backfilled ITO-glasses were rinsed with universal buffer and ultra-pure water, dried with gase nitrogen and stored under vacuum in a dessicator until use.

2.2.3. Electron Beam Lithography

Protein (K-casein or fibronectin) coated ITO-glasses were patterned by electron beam lithography using a Raith E-line system with a high precision interferometric stage (Raith GmbH, Dortmund, Germany). Firstly, vacuum operation was processed to open the gate of device for sample placement. "Unload" operation was started by "Navigator" option of Raith E-line software. System pressure was balanced by release of N_2 from gase nitrogen tank to main chamber of device. Stage was taken out and ITO-glass sample was placed onto this stage. Stage was placed into device again. "Load" operation was started by "Navigator" option of Raith E-line software and N_2 flow was stopped. During the loading, vacuum pump was operated to reduce the vacuum pressure to ~2-5 x 10^{-6} mBar in the chamber. Dtermination of sample position was performed. Precision adjustment was provided by "stigmation" and "aperture" optimization. Moreover, sensitivity of electron gun targeting was enhanced by "writefield alignment" calibration. Average working distance was calculated from two distant points. Current was measured at "Faraday Cup" position with setting of average working distance. The accelerating voltage was set to 5 kV and aperture size to 30 μm. Patterns were designed using Raith software in GDSII format. Line exposure mode was used with 2, 4 and 8 μm step sizes. Line exposure dose was set to 1600 pAs cm^{-1} and dwell times were assigned to system.

2.2.4. Cell Incubation on Patterned ITO Glasses

Dimensions of ITO-glass were 75 mm in length and 25 mm in width that fit into 100 mm petri dish. When the cells were ready for passage (confluency > 80%), the cells could be used for experiments. For experiments, cells were starved in serum free medium

(L15-BSA) at 37°C and 5% CO_2 for 2 hours in incubator. ITO-glasses were also kept in L15-BSA to adapt their surfaces at 37°C and 5% CO_2 for 1 hour in incubator. Cells were trypsinized and cultured in their medium on ITO-glass with 1.8 x 10^6 cells per 100 mm petri dish at 37°C and 5% CO_2 for 18 hours.

2.2.5. Cell Adhesion under Flow

SU-8 masters were fabricated with height 1 mm, width 13 mm and length 50 mm by UV lithography using SU-8 2075. These masters were used for PDMS molding. PDMS base was mixed with curing agent at the ratio of 10:1 and degassed by dessicator. While degassing process was carried out, washing of SU-8 master with EtOH and H_2O and cleaning with demolding agent were done. PDMS mixture were poured onto SU-8 master and was left for polymerization at room temperature for at least 2 days. After polymerization, channels were provided by separation of polymerized PDMS from the wafer. PDMS channels inner faces were treated to UV-ozone to clean and self-activate surface. Afterwards. patterned ITO-glass surfaces were caged by constructed PDMS (polydimethylsiloxane) channels. Flow system was set up by connection of all equipments as a serial coordination with the help of silicon tubes. Peristaltic pump provided the flow and allowed to continuous circulation of cell suspension in the system (Figure 2.1). Heater and water bath supplied the conservation of appropriate temperature, during the experiment 37°C, in addition magnetic stir bars prevented the precipitation of cells in suspension. Flow rate was 235 µl/min for shear stress 0.02 dyn/cm^2 and applied for 24 hours. Cells were suspended in L15 serum which was formulated for use in carbon dioxide free systems. Status of cells in channel was observed by phase-contrast microscope. At the end of 24 hours flow, adhered cells were fixed and stained according to immunofluorescence procedure and images were captured under fluorescence microscope.

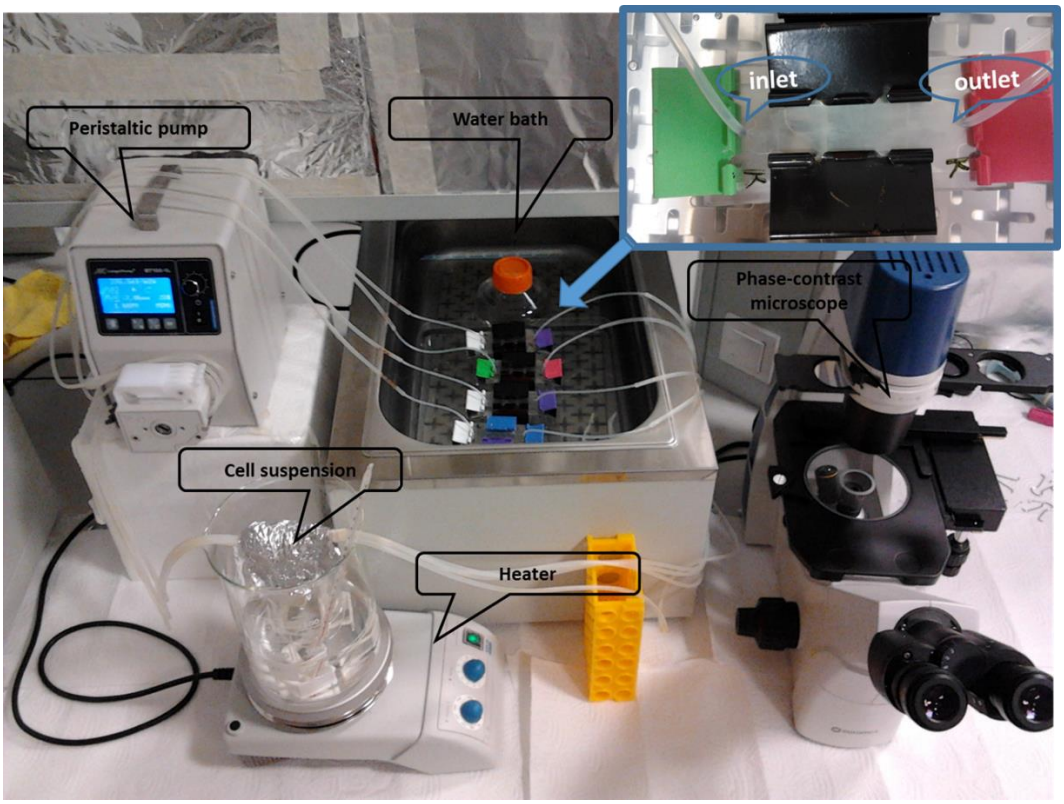

Figure 2.1. Flow system. Peristaltic pump, cell suspension, heater, water bath, PDMS-caged patterned ITO-glass and phase-contrast microscope were shown. Connection of channel to system from inlet and outlet holes by silicon tubes was shown at the top-right corner.

2.2.6. Immunofluorescence

After 18 hours incubation, surfaces with cells were fixed with treatment of 4% paraformaldehyde (in 1X PBS) at room temperature for 30 minutes. Samples were washed gently with 1X PBS, for 5 minutes, thrice. Fixed samples were permeabilized with 0.1% Triton X-100 (in 1X PBS) for maximum 5 minutes. Samples were washed gently with 1X PBS, for 5 minutes, thrice. The samples were blocked with 1% bovine serum albumin for 1 hour. The samples were incubated with 1^{st} antibodies in blocking solution at room temperature for 1 hour. 1^{st} antibodies were fibronectin and vinculin specific. The samples were washed with 1X PBS-three times for 5 minutes. The samples were incubated with 2^{nd} antibodies in blocking solution at room temperature for 50 minutes (light protected), in order to stain actin cytoskeleton we also added phalloidin 647 or phalloidin 350 in 2^{nd} antibody solution. 2^{nd} antibodies were Alexa488 and Alexa555 fluorophore conjugated for fibronectin and vinculin, respectively. The samples were washed for three times for 5 minutes with 1X PBS. The samples were mounted by

ProLong antifade reagents. The samples were imaged using an Olympus epifluorescence microscope with a 100X oil immersion objective.

2.2.7. Image Analysis

All image processing and analysis steps were performed via ImageJ. Raw fluorescent images were in RGB format and 8-bit type, firstly images were splitted to their channels to red, green and blue. Dominant channel was used for processing and analysis, for example vinculin was stained with Alexa555 conjugated antibodies and in this case dominant channel of vinculin images was red channel.

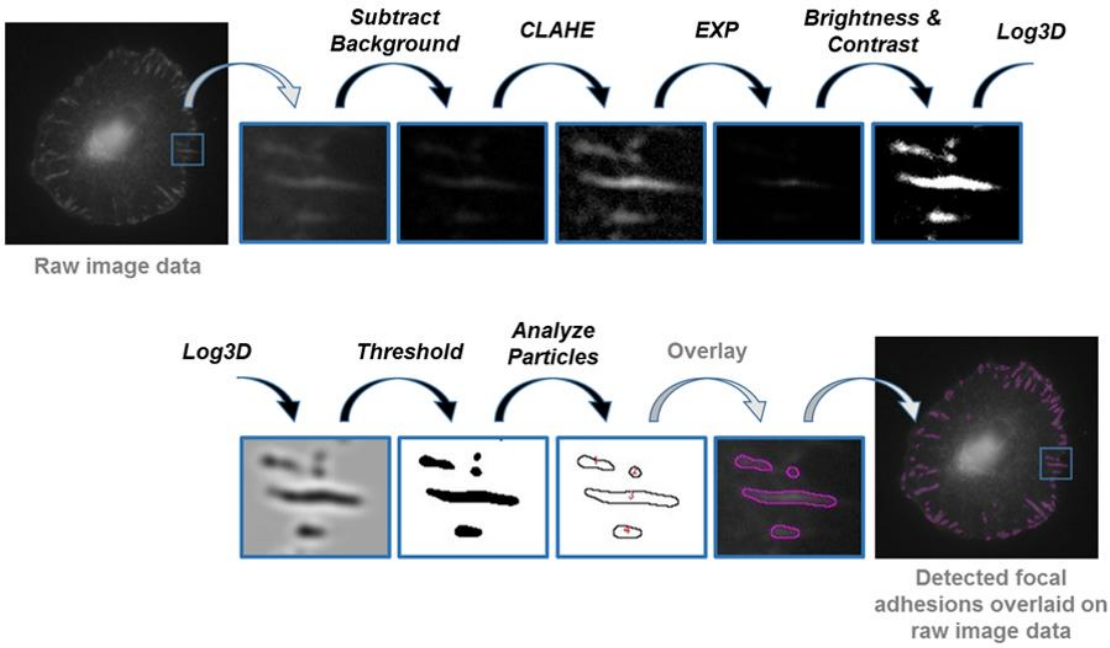

Figure 2.2. Graphical abstract of step-by-step quantitative analysis of focal adhesions by sequential run of plugins of the ImageJ program (Source: Horzum, Ozdil, & Pesen-Okvur, 2014b).

For focal adhesion analysis (Figure 2.2), background of vinculin images was eliminated by running SUBTRACT BACKGROUND command with SLIDING PARABOLOID option with the ROLLING BALL radius set to 50 pixels. Local contrast of images was enhanced by running CLAHE (Contrast Limited Adaptive Histogram Equalization) with defined parameters which were block size=19, histogram bins=256, maximum slope=6, no mask and fast. To further minimize the background, images were exposed to mathematical exponential (EXP). Brightness and contrast of images were adjusted automatically by running BRIGHTNESS & CONTRAST command. Images were filtered by running Log3D (Laplacian of Gaussian or Mexican Hat) filter with defined parameters which were sigma X=5 and sigma Y=5. Images were converted to binary images by running THRESHOLD command with default method and automatically adjustment. Lastly, execution of ANALYZE PARTICLES command provided the counting and measuring of objects or particles in manually selected regions on images. Here, particle analyzer counted and measured the particles according to user-defined parameters which were size=50-infinity and circularity=0.00-0.99. For cell area and cell aspect ratio analysis, actin images were used. Cell contours were manually drawn and MEASURE command was run.

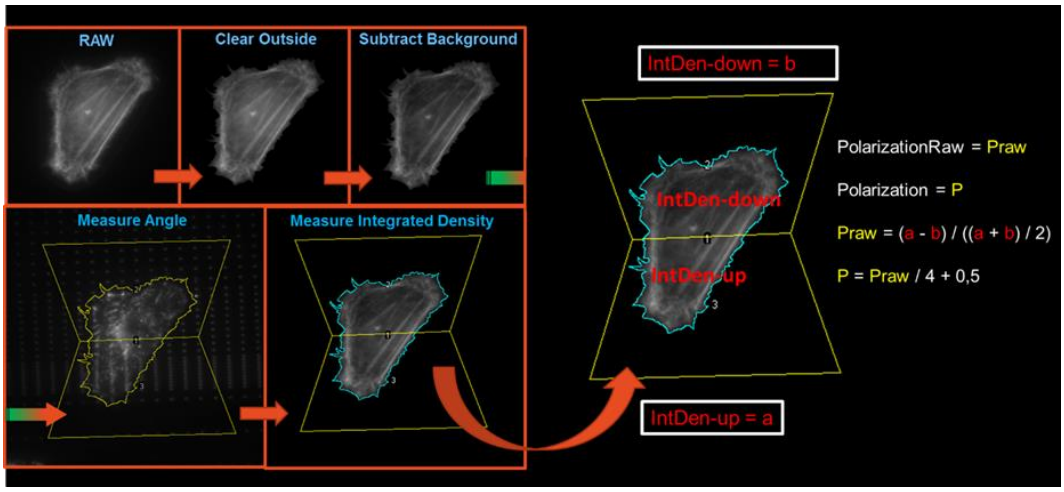

Figure 2.3. Graphical abstract and normalization flow sheet of quantitative analysis of actin by sequential run of plugins of the ImageJ program.

Analysis of actin polarization was done by following image analysis steps and using a normalization formula (Figure 2.3). In this case, raw actin images were used. In first step CLEAR OUTSIDE command was run to eliminate redundant background by selection of region of interest, cell boundaries.. Afterwards, background of actin images was further eliminated by running SUBTRACT BACKGROUND command with SLIDING PARABOLOID option with the ROLLING BALL radius set to 500 pixels. In the third step, selected region of interest was partitioned from the center according to fibronectin pattern degree. Partitioned regions were used to measure integrated densities of actin images as two separate region on the cell. Polarization values were calculated from measured integrated densities by normalization formula.

CHAPTER 3

RESULTS AND DISCUSSION

3.1. Determination of Proper Parameters of Electron Beam Lithography

ITO is a conductive material which is essential for discharging during the EBL writing. ITO coating forms a thin layer on the glass surface and this slightly effect the transparency can be ignored (Figure 3.1). APTES is a hydrophobic molecule and treatment of APTES forms functional and hydrophobic surface over the ITO coated glass. After APTES coating, surface can be coated with proteins. Desirable patterning of protein-coated ITO-glass surfaces were possible with appropriate intervention of electron gun to assigned locations with the best fit parameters. ITO-glasses were tested for direct patterning of protein coated surfaces by area exposure mode (Figure 3.2). Area doses ranging from 5 to 80 μC cm^{-2} were tested. Exposed areas were backfilled with FN and immunostaining of these areas by FN immunospecific antibodies provided the detection of fluorescent intensities to determine the effect of dose factor. Low dose values were enough to initiate FN binding to exposed areas but efficient coverage of the exposed areas by FN was observed at area doses of 65 μC cm^{-2} and higher. Here, it was clear that ITO-glass could be used as substrate for EBL with determination of best fit parameters. Results showed that K-casein coated ITO-glass could be directly patterned with EBL and exposed areas were available for selectively binding of FN molecules.

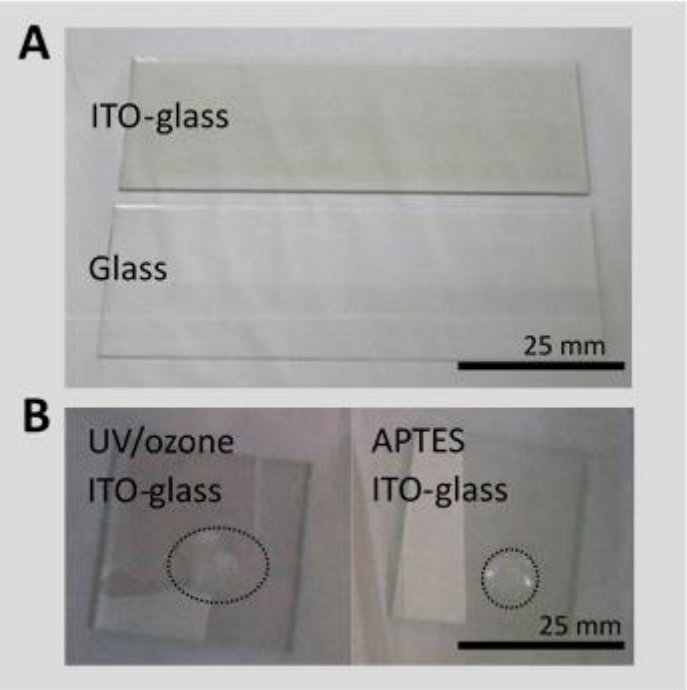

Figure 3.1. Suitability of ITO-glass as an EBL substrate. A: Transparency of ITO-glass. B: Hydrophobicity of ITO-glass surface after UV/Ozone cleaning and APTES coating. Scale bars show 25 mm.

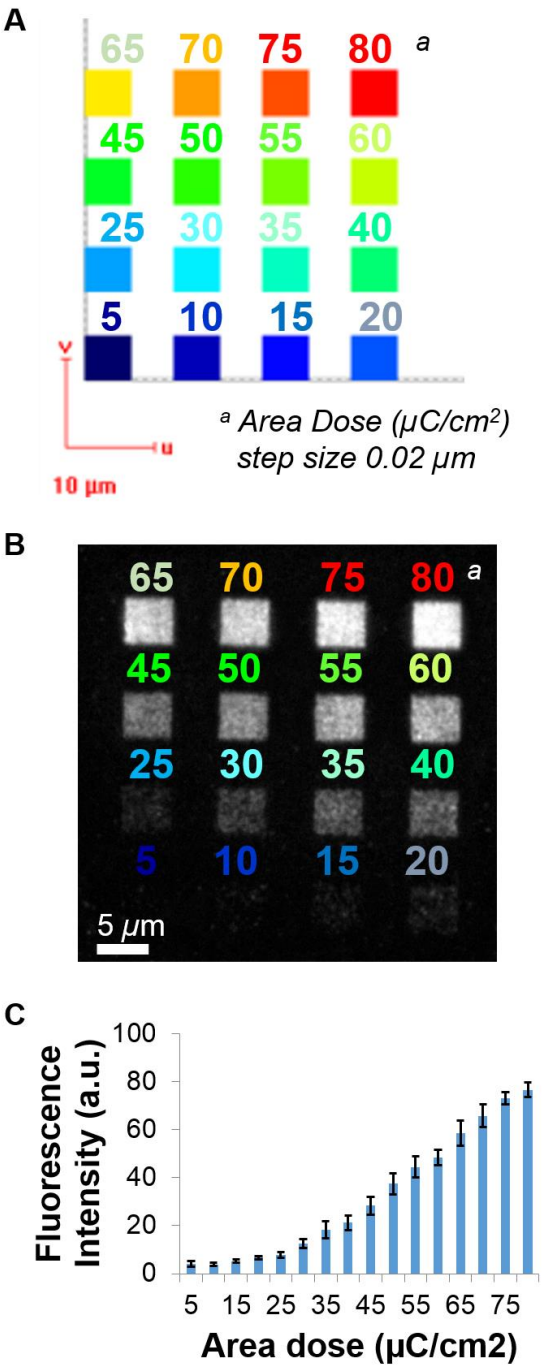

Figure 3.2. Area exposure mode was tested on K-kasein-coated ITO-glass surfaces within defined dose spectrum. A : Designed area pattern by EBL software, each square has a size of 5x5 µm^2. Each square was colored corresponding to magnitude of applied area dose in a same manner. B : Fluorescent image of exposed areas which were backfilled with fibronectin and immunostained. C : Graph of obtained fluorescent signal connected with applied area dose. Accelerating voltage 5 kV, aperture size 30 µm.

We aimed to pattern FN nanodots on the K-casein coated ITO-glass surface with defined micrometer scale spaces. Dot exposure mode was quitely time-consuming, especially when we wanted to pattern approximately whole surface of a ITO-glass. Because of this, firstly line exposure mode was tested to determine functionality of this mode to pattern nanodots within three different dose values, 1000, 100 and 10 pAs/cm (Figure 3.3). In line exposure mode, it was observed that FN nanodots could be fabricated by desired spacings depending on defined step size. Moreover, we recognized that line exposure mode was also dose-dependent for proper function because doses of 100 and 10 pAs/cm were not sufficient to get effective fluorescence signals over dots by FN binding. Fortunately, line exposure mode was a good choice to overcome time limitation that there was a significant reduction for exposure time.

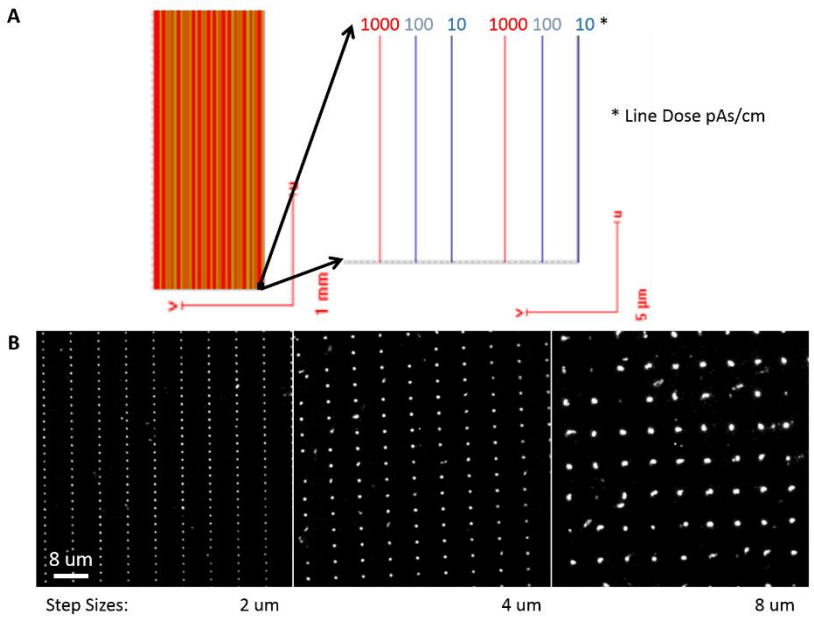

Figure 3.3. Line exposure mode was tested on K-kasein-coated ITO-glass surfaces within defined dose spectrum. A : Designed line pattern by EBL software. One corner of the pattern is magnified to show individual lines. Each line was colored corresponding to applied line dose. B : Fluorescent image of exposed lines which were backfilled with fibronectin and immunostained. 100 and 10 pAs/cm line doses were not observed because of insufficient fluorescence intensities. Accelerating voltage 5 kV, aperture size 30 µm. Step size changed distance between dots.

Line dose dependence of direct patterning of nanodots was tested extensively by profiling of fluorescence intensity and nanodot diameter, additionally two different

aperture sizes, 7,5 and 30 μm were tested (Figures 3.4, 3.5 and 3.6). At 30 um aperture, line doses ranging from 200 to 3200 pAs cm^{-1} were tested. At 7.5 μm aperture, line doses ranging from 2 to 1000 pAs cm^{-1} were tested. In each case, we observed that diameters of resulting FN nanodots larger for 30 μm aperture than 7.5 μm aperture with comparision of same dose levels. For 30 μm aperture, we got similar diameters of FN nanodots for different doses (588 ± 6 nm for 3200 pAs cm^{-1} ; 538 ± 14 nm for 1600 pAs cm^{-1} ; 497 ± 18 nm for 800 pAs cm^{-1}). Fluorescent profiling showed that electron dose over 400 pAs cm^{-1} provided increasing of the efficiency of backfilling. For 7.5 μm aperture, diameters of resulting nanodots significantly increased as the electron dose increased (238 ± 11 nm for 212 pAs cm^{-1}; 653 ± 18 nm for 1000 pAs cm^{-1}). Here, fluorescent profiling showed that threshold dose was 200 pAs cm^{-1} to initiate the backfilling of surfaces for 7.5 μm aperture. Larger diameters of FN nanodots provide an increase of cell adhesion on patterned surfaces (Pesen & Haviland, 2009). As a result of this, EBL was performed in line exposure mode with best fit parameters which were aperture size = 30 μm, line exposure dose = 1600 pAs cm^{-1}. Micrometer scale spacings between nanodots were arranged by step size definition at the one of the axes and determination of invidual line spacings on EBL drawing software at the other axes.

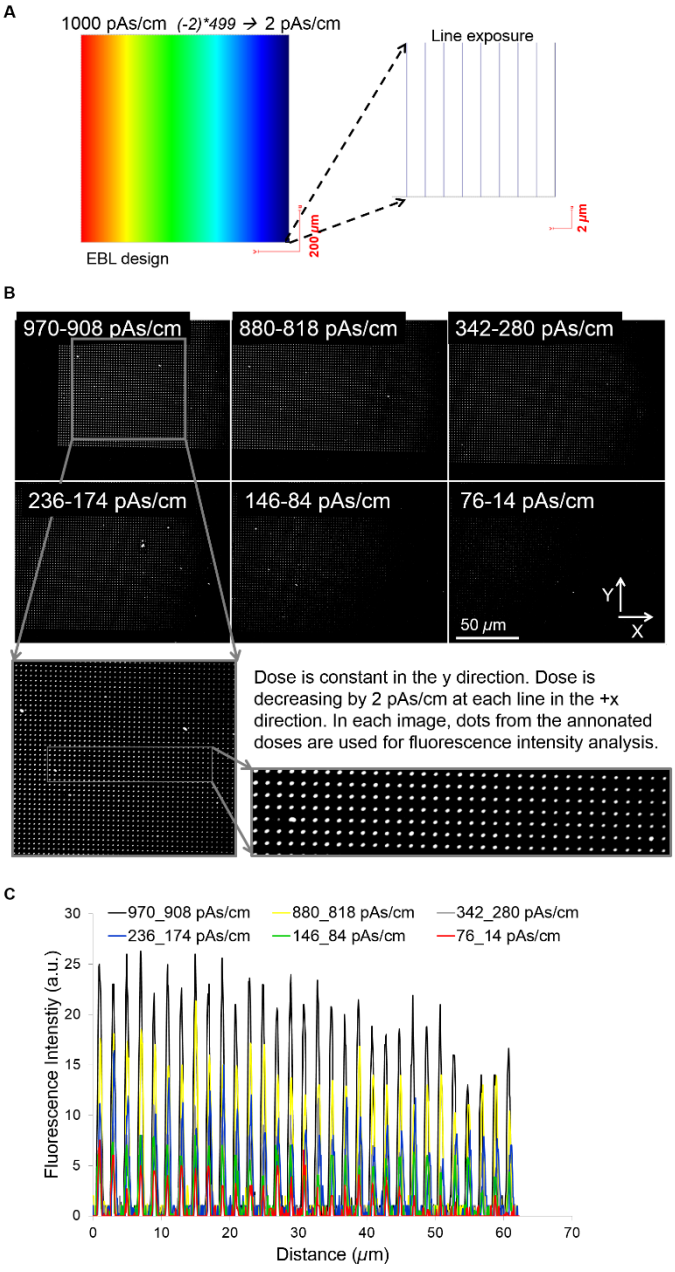

Figure 3.4. Line dose test for determination of threshold dose value on K-casein-coated ITO-glass surfaces. A : Designed line pattern by EBL software. One corner of the pattern is magnified to show individual lines. Each line was colored corresponding to applied line dose. B : Fluorescent images of exposed lines which were backfilled with fibronectin and immunostained. Initial dose was 1000 pAs/cm decreased by 2 pAs/cm for following line, gradual decline was observed on fluoresence intensity of dots along x axis. C : Representation of fluorescent signal values along the axis by distance. Accelerating voltage 5 kV, aperture size 7.5 µm.

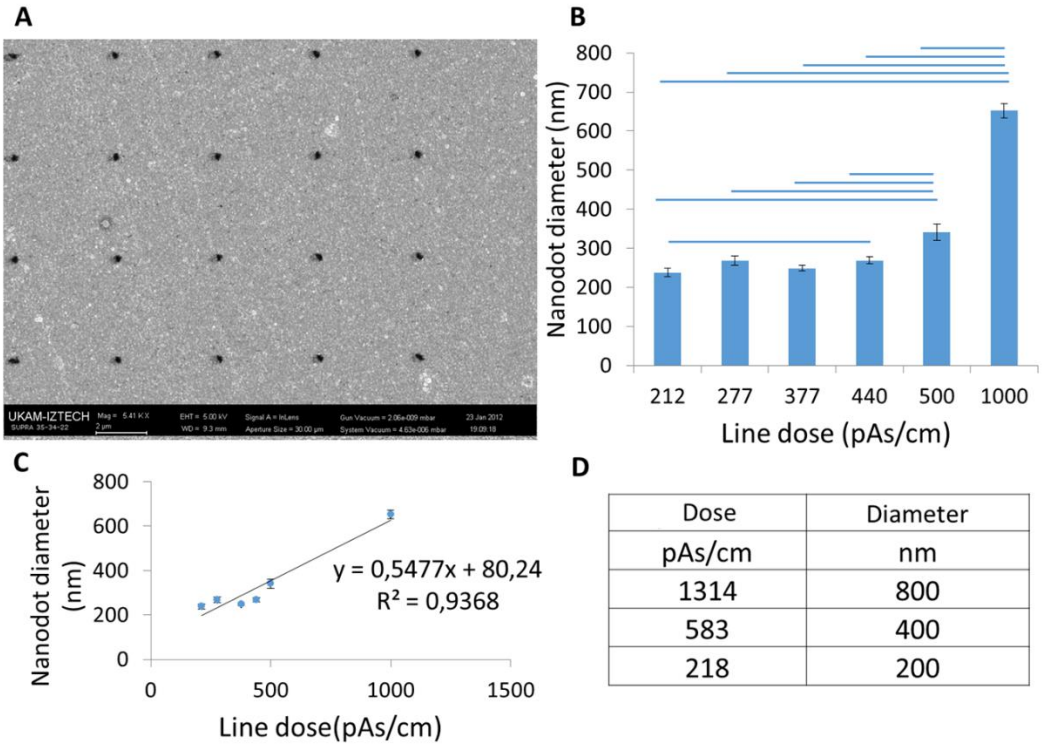

Dose	Diameter
pAs/cm	nm
1314	800
583	400
218	200

Figure 3.5. Line dose dependence of nanodots was reflected as diameter variation on K-casein-coated ITO-glass surfaces. A : SEM image of part of sample. B : Nanodot diameter corresponding to applied line dose (n = 4 – 20 per dose). Horizontal solid lines show data with statistically significant differences with $p<0.05$ for two-tailed t-test. C : Nanodot diameter increased with the applied dose. D : According to correlation, anticipated diameters for defined doses were calculated. Accelerating voltage 5 kV, aperture size 30 μm.

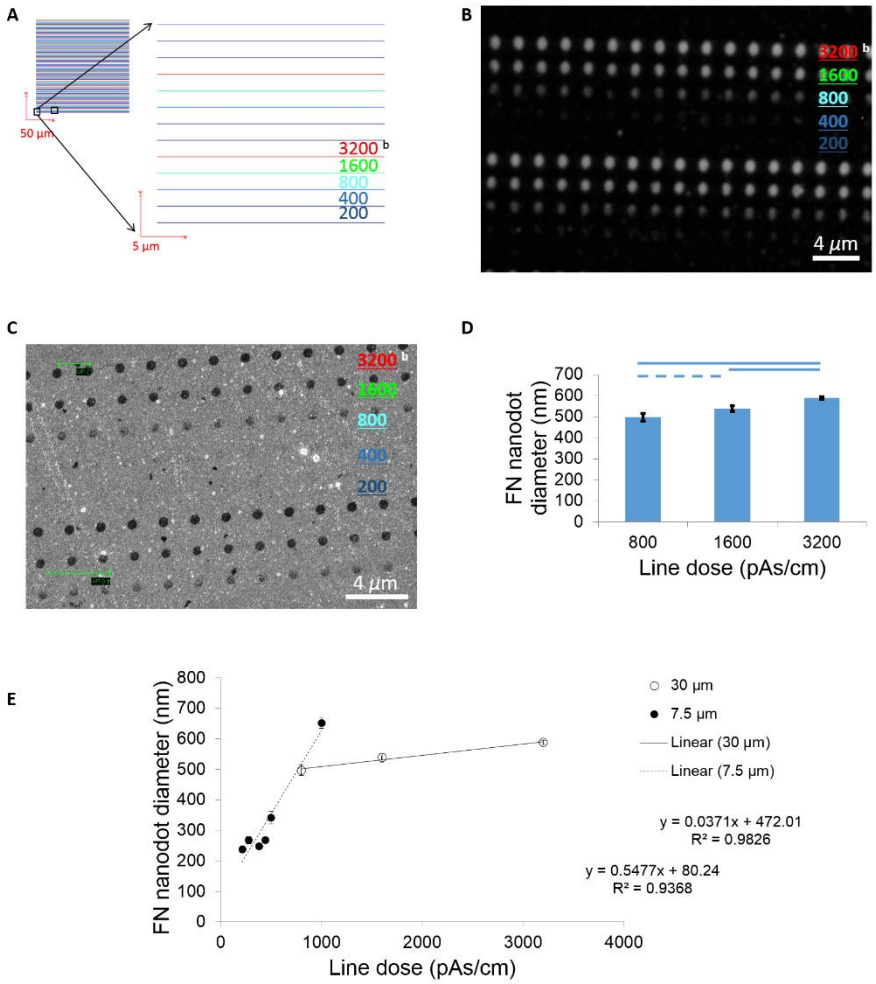

Figure 3.6. Line exposure mode with different doses over the threshold dose results in nanometer scale fibronectin nanodots by using a micrometer scale step size. A : Line pattern drawn in EBL software. One corner of the pattern is magnified to show individual lines. B : Immunofluorescence image of FN nanodots on K-casein background corresponding to pattern in (A). Sample was stained with FN specific antibodies. Fluorescence intensity of FN immunostaining increased as the applied dose increased. C : SEM image of the sample in (B). 30 µm aperture was used for EBL. D : Diameter of FN nanodot increased as the applied electron dose increased. Horizontal solid and dashed lines show data with statistically significant differences with $p < 0.05$ for two-tailed and one-tailed t-tests, respectively. E : FN nanodot diameter increased with the applied dose but with different correlations for 7.5 and 30 µm apertures (n= 4 – 21 per dose).

3.2. Cell Adhesion on FN Nanodots with Micrometer Spacings under Static Conditions

Each type of cells, MDA-MB-231 and MCF10A, were cultured on K-casein and fibronectin coated ITO-glass surfaces. The number of cultered cells was same for each sample, 1.8 x 10^6 cells per sample. In these cases, we observed that fibronectin coated surfaces were appropriate for cell adhesion rather than K-casein coated surfaces. K-casein was a blocking agent which did not have any relationship with extracellular matrix proteins. As a result of this, cells did not attach to the K-casein surfaces or attached cells did not show high number of adhesive structures which are focal adhesion in this circumstance (Figure 3.7-11).

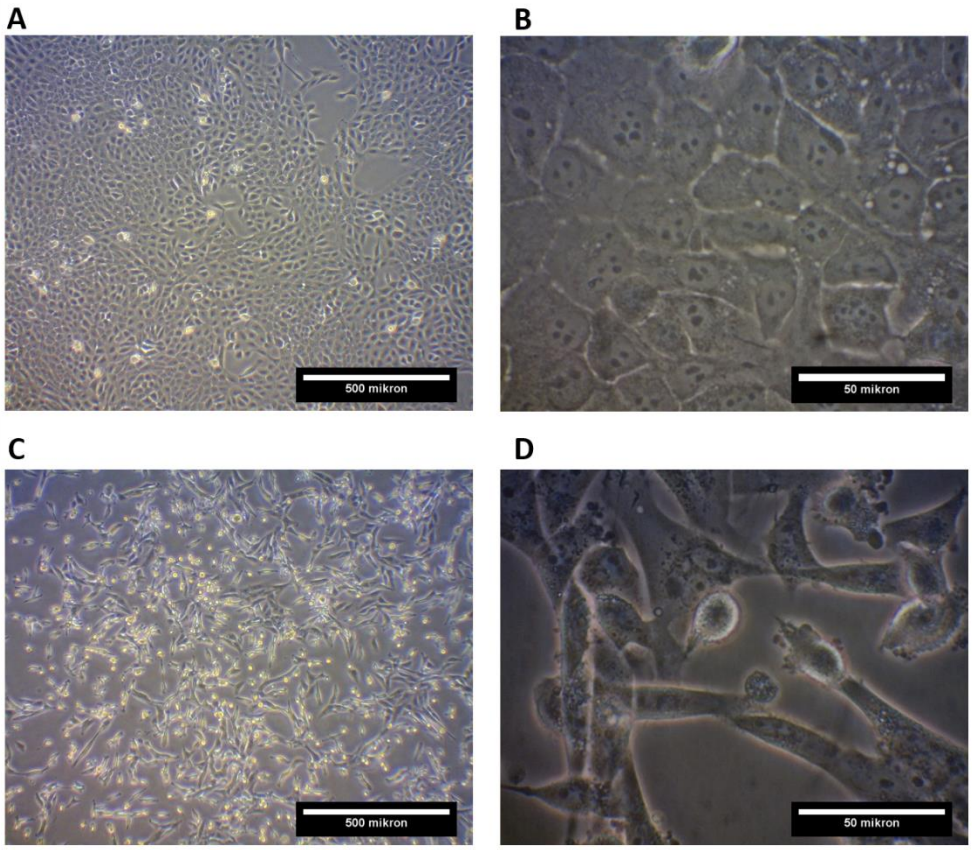

Figure 3.7. Phase-contrast images of used cells. A and B : Normal breast epithelial cells (MCF10A) at 4X and 40X magnifications, respectively. C and D : Cancer breast epithelial cells (MDA-MB-231) at 4X and 40X magnifications, respectively.

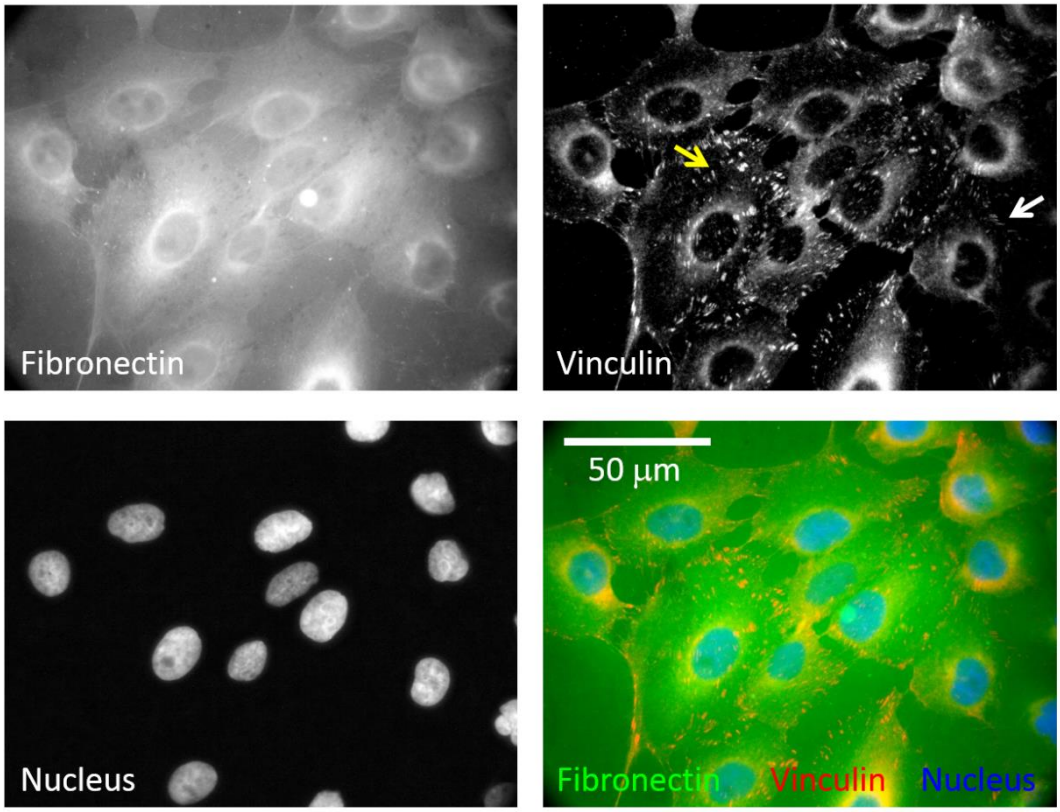

Figure 3.8. Immunofluorescence images of MCF10A cells cultured on fibronectin coated ITO-glass surfaces. Cells were starved for 2 hours, trypsinized and cultured for 18 hours. From left-to-right and top-to-bottom, images of fibronectin, vinculin, DAPI stainings and their merged case. In vinculin image, arrows show representative focal adhesions.

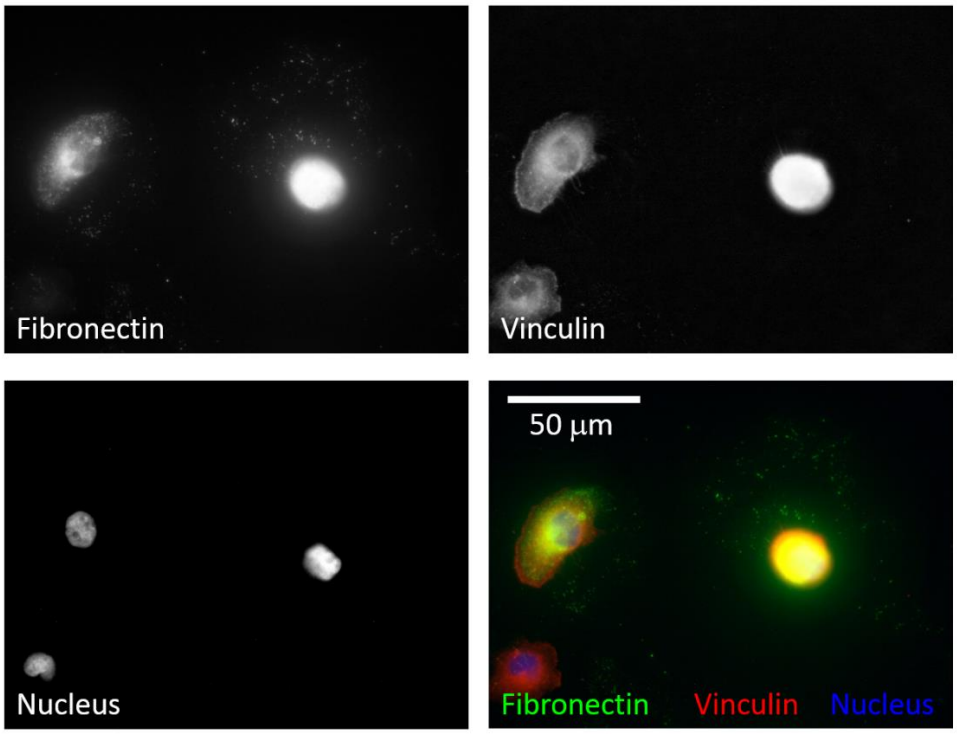

Figure 3.9. Immunofluorescence images of MCF10A cells cultured on K-casein coated ITO-glass surfaces. Cells were starved for 2 hours, trypsinized and cultured for 18 hours. From left-to-right and top-to-bottom, images of fibronectin, vinculin, DAPI stainings and their merged case.

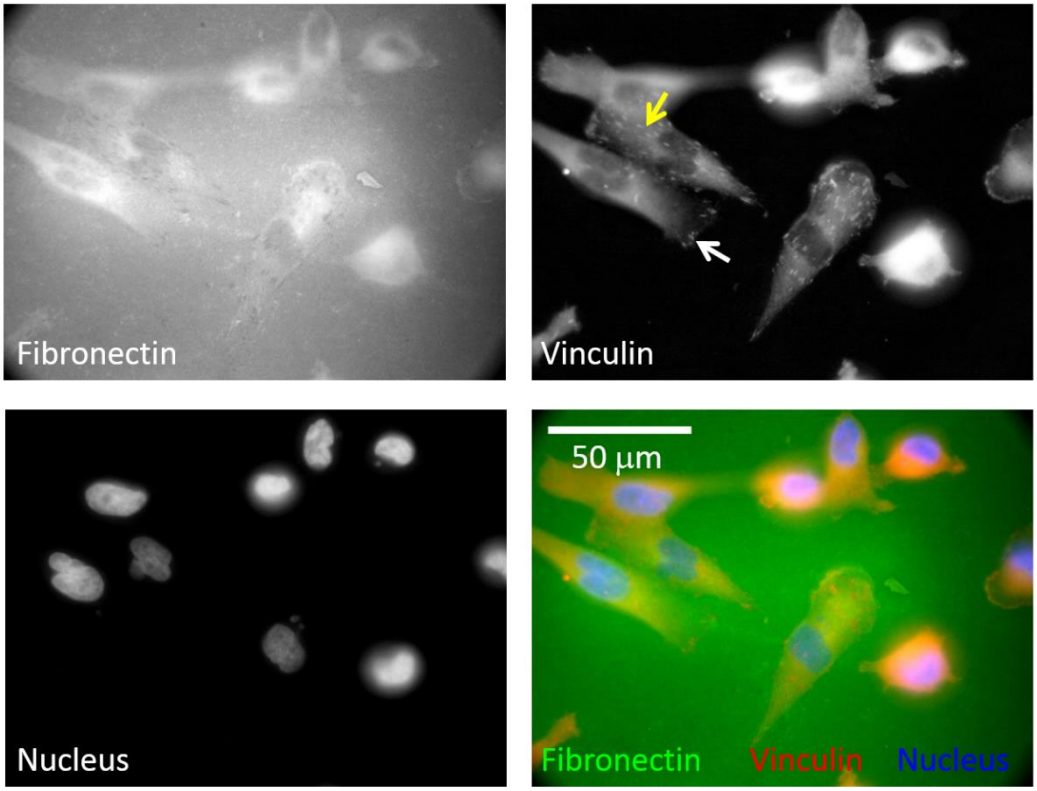

Figure 3.10. Immunofluorescence images of MDA-MB-231 cells cultured on fibronectin coated ITO-glass surfaces. Cells were starved for 2 hours, trypsinized and cultured for 18 hours. From left-to-right and top-to-bottom, images of fibronectin, vinculin, DAPI stainings and their merged case. In vinculin image, arrows show representative focal adhesions.

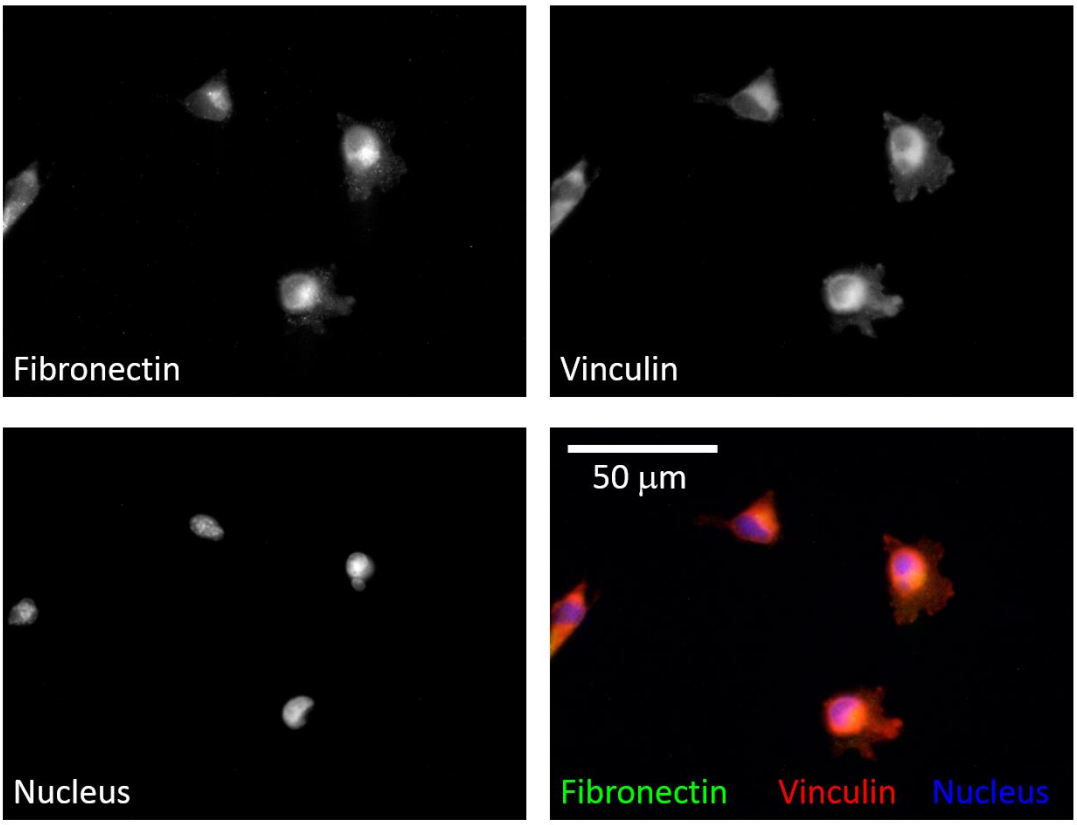

Figure 3.11. Immunofluorescence images of MDA-MB-231 cells cultured on K-casein coated ITO-glass surfaces. Cells were starved for 2 hours, trypsinized and cultured for 18 hours. From left-to-right and top-to-bottom, images of fibronectin, vinculin, DAPI stainings and their merged case.

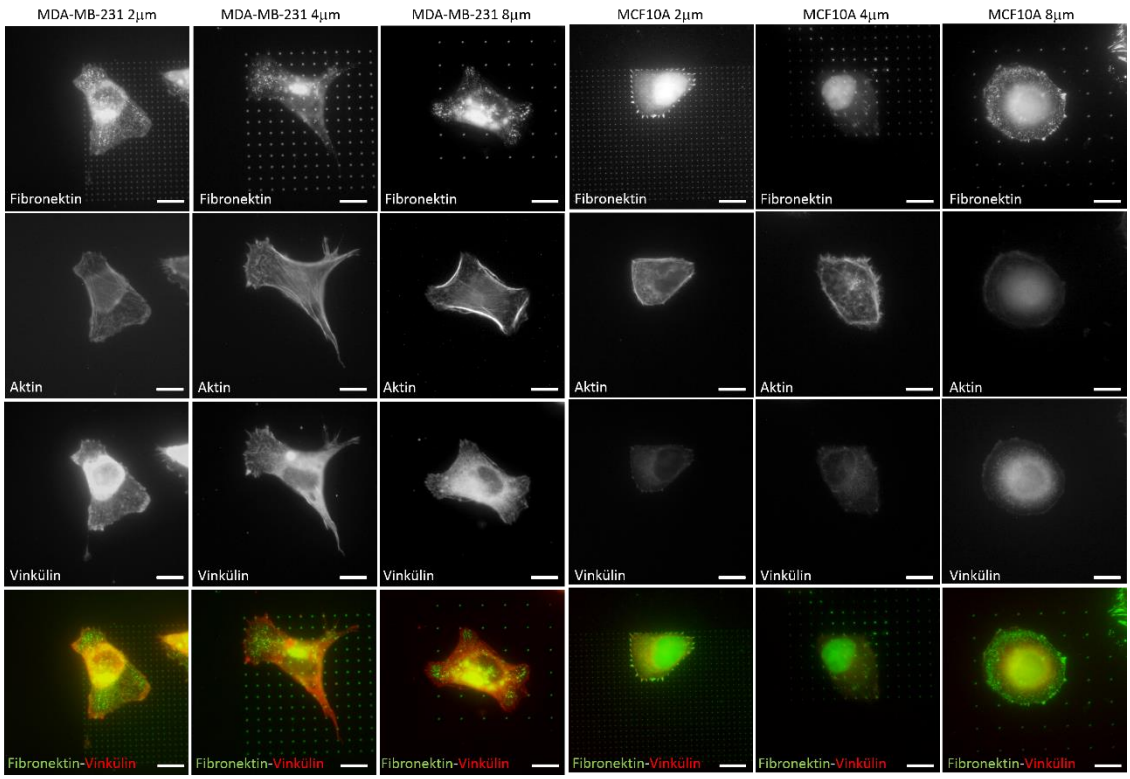

Figure 3.12. Immunofluorescence images of cells on patterned ITO-glass surfaces. Top-to-bottom, horizontal panels show fibronectin, actin, vinculin and merged images, respectively. Left-to-right, vertical panels show 2, 4 and 8 um spacings in a order of first thriple for MDA-MB-231 cells and second thriple for MCF10A cells, respectively. Scale bars show 8 μm.

MDA-MB-231 cell area decreased as nanopattern spacing increased. MCF10A cell area did not change significantly with nanopattern spacing. There were not any significant differences between areas of MDA-MB-231 and MCF10A cells on similar surfaces. MCF10A cells and MDA-231 cells spread larger areas on FN surfaces (Figure 3.13). MDA-MB-231 cell aspect ratio did not change significantly with nanopattern spacing. MCF10A cell aspect ratio increased on nanopatterning surfaces in comparison with control surfaces. There were significant differences between aspect ratios of MDA-MB-231 and MCF10A cells on only control surfaces. In general perspective, MDA-MB-231 cells were more elongated or asymetric in comparision with MCF10A cells on similar surfaces (Figure 3.14).

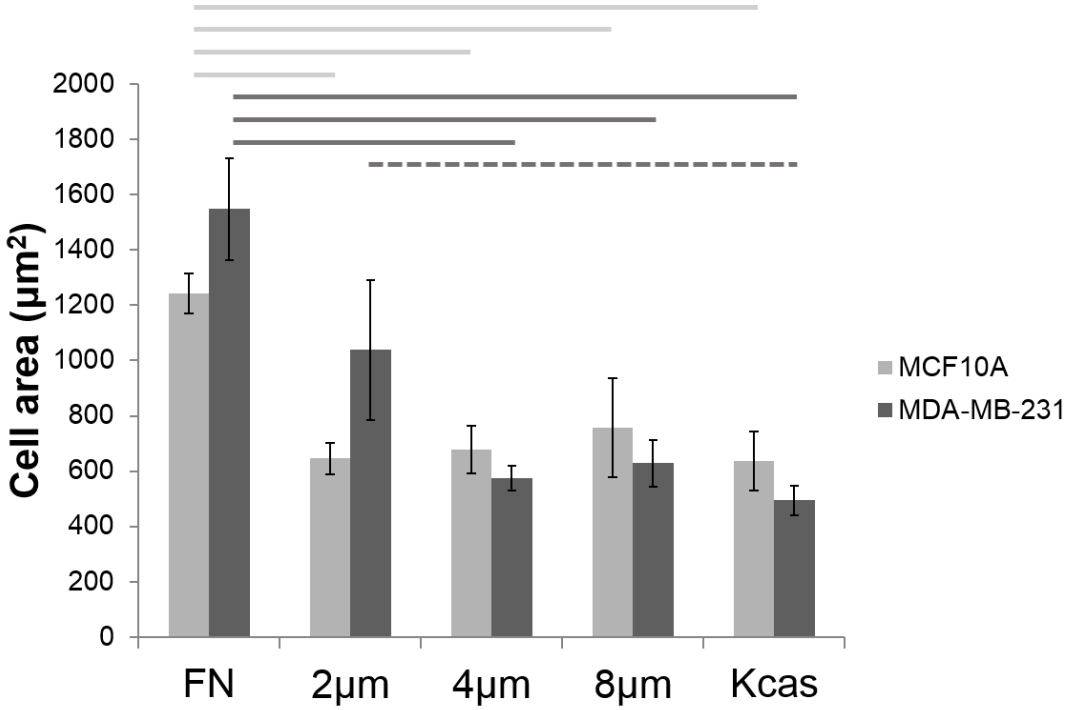

Figure 3.13. Alteration of cell area on K-casein control, FN control and nanopattern spacings surfaces. Horizontal solid and dashed lines show data with statistically significant differences with $p<0.05$ for two-tailed and one-tailed t-tests, respectively. (n = 9-70 cells).

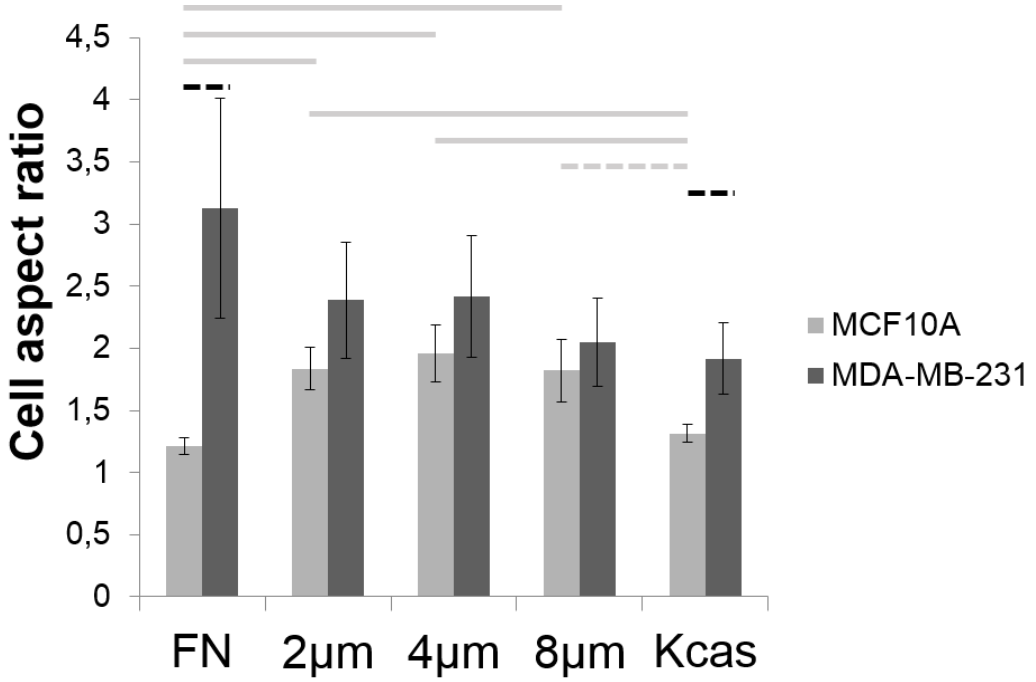

Figure 3.14. Alteration of cell aspect ratio on K-casein control, FN control and nanopattern spacings surfaces. Horizontal solid and dashed lines show data with statistically significant differences with $p<0.05$ for two-tailed and one-tailed t-tests, respectively. (n = 9-70 cells).

Each cell type showed that number of FAs on FN nanodots decreased as nanopattern spacing increased (Figure 3.15). On FN control surfaces, MDA-MB-231 cells have large number of FAs with a significant difference as compared with MCF10A cells. Nanopattern surfaces with 4 µm spacings were more distinctive for cell behaviour, so cells have significant differences for on and off status with regard to FA number in itself and cells also have significant difference for their FA off numbers between each other.

Alteration of FA area is dependent to surface for each type of cells (Figure 3.16). FA area increased as nanopattern spacing increased for both cells. In this case, individual FAs enforced on more distant FN nanodots such as 8 µm. There were significant differences between FA areas of MDA-MB-231 and MCF10A cells for off states of 2 and 4 µm spacings.

Total FA areas decreased on FN nanodots as nanopattern spacing increased (Figure 3.17). Nanopattern surfaces with 4 µm spacings were more distinctive for cell behaviour, so cells have significant differences for off status with regard to total FA area between each other.

Each cell type had different circularities for their FA between on and off status (Figure 3.18). FA on FN nanodots was more linear than FAs between FN nanodots. It was clear that FAs on FN nanodots elongated and maturated with the expected interaction of integrins on fibronectins, as a result of this, FAs grew away from circular structures.

For distribution graph, FA area and circularity graphes was also supportive that when FAs area increased, FA circularity decreased (Figure 3.19). These data showed that maturation of FAs could be observed by increasing of their individual areas or decreasing of their individual circularities.

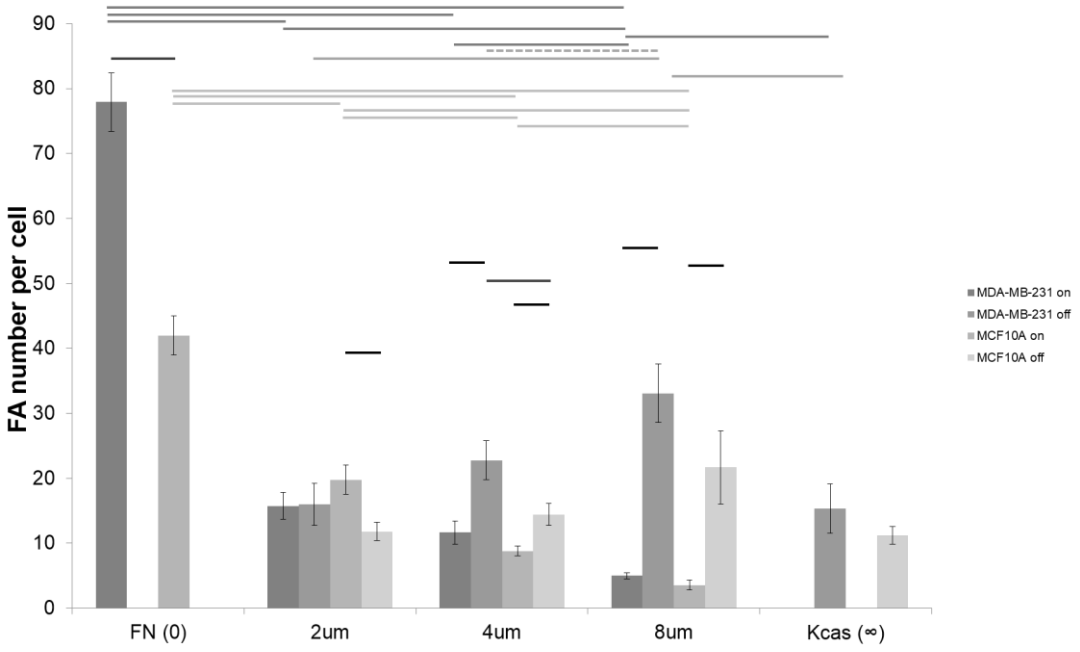

Figure 3.15. Alteration of number of FAs per cell on K-casein control, FN control and nanopattern spacings surfaces. FAs on FN nanodots are on and FAs between FN nanodots are off. FN coated surfaces have all on FAs and K-casein control surfaces have all off FAs. Horizontal solid and dashed lines show data with statistically significant differences with $p<0.05$ for two-tailed and one-tailed t-tests, respectively. (n = 9-70 cells).

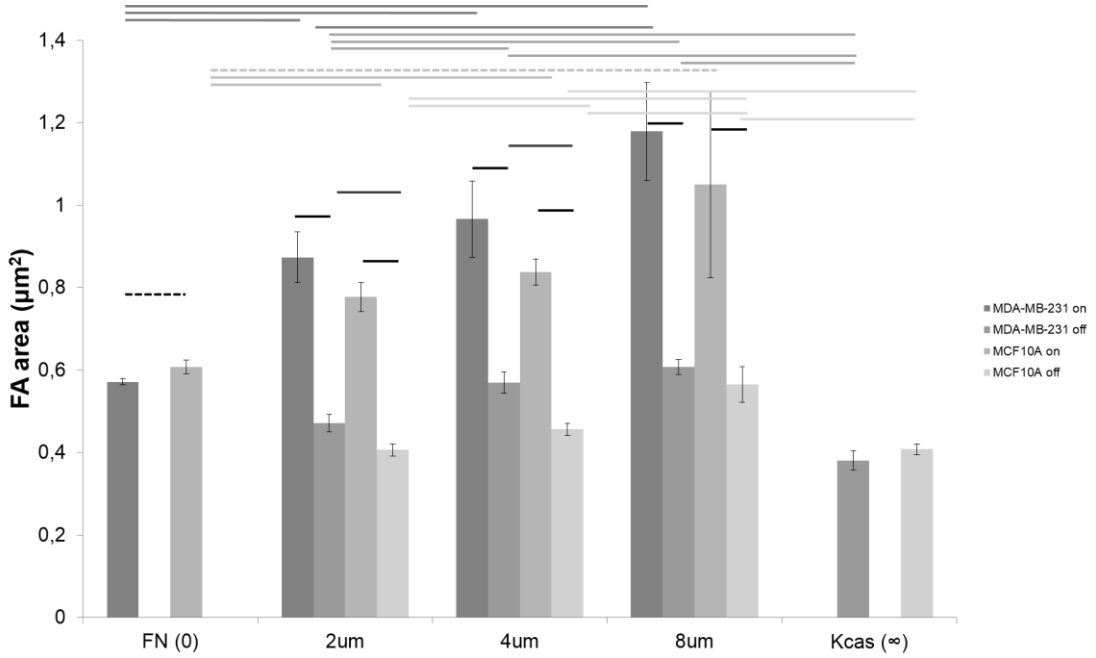

Figure 3.16. Alteration of average area of FAs on K-casein control, FN control and nanopattern spacings surfaces. FAs on FN nanodots are on and FAs between FN nanodots are off. FN coated surfaces have all on FAs and K-casein control surfaces have all off FAs. Horizontal solid and dashed lines show data with statistically significant differences with $p<0.05$ for two-tailed and one-tailed t-tests, respectively. (n = 9-70 cells).

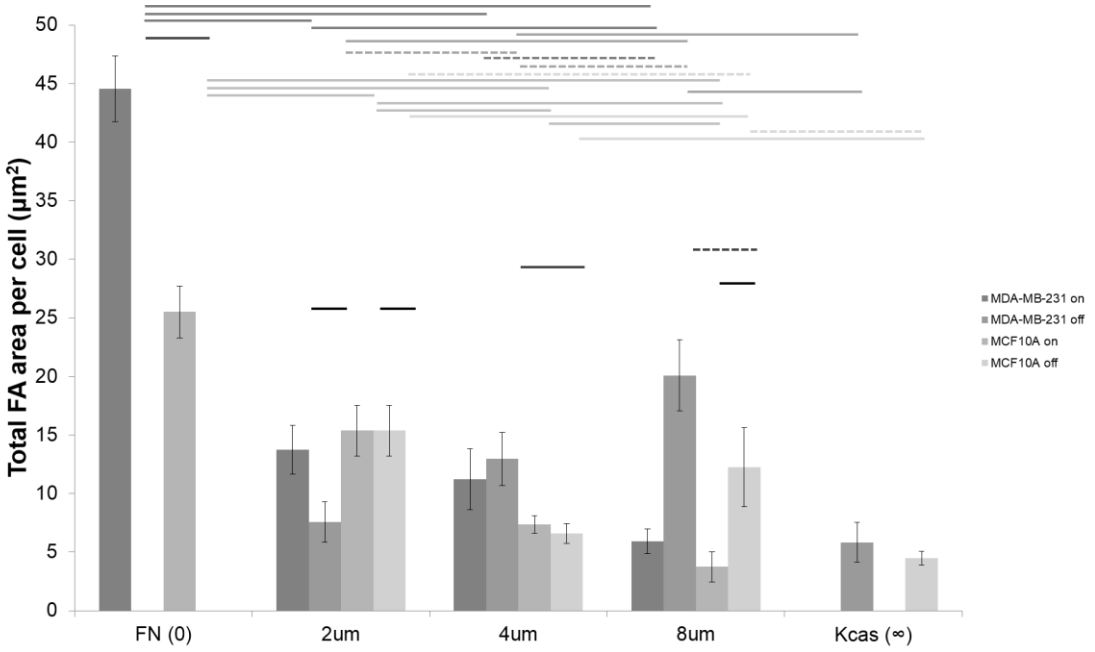

Figure 3.17. Alteration of total area of FAs per cell on K-casein control, FN control and nanopattern spacings surfaces. FAs on FN nanodots are on and FAs between FN nanodots are off. FN coated surfaces have all on FAs and K-casein control surfaces have all off FAs. Horizontal solid and dashed lines show data with statistically significant differences with $p<0.05$ for two-tailed and one-tailed t-tests, respectively. (n = 9-70 cells).

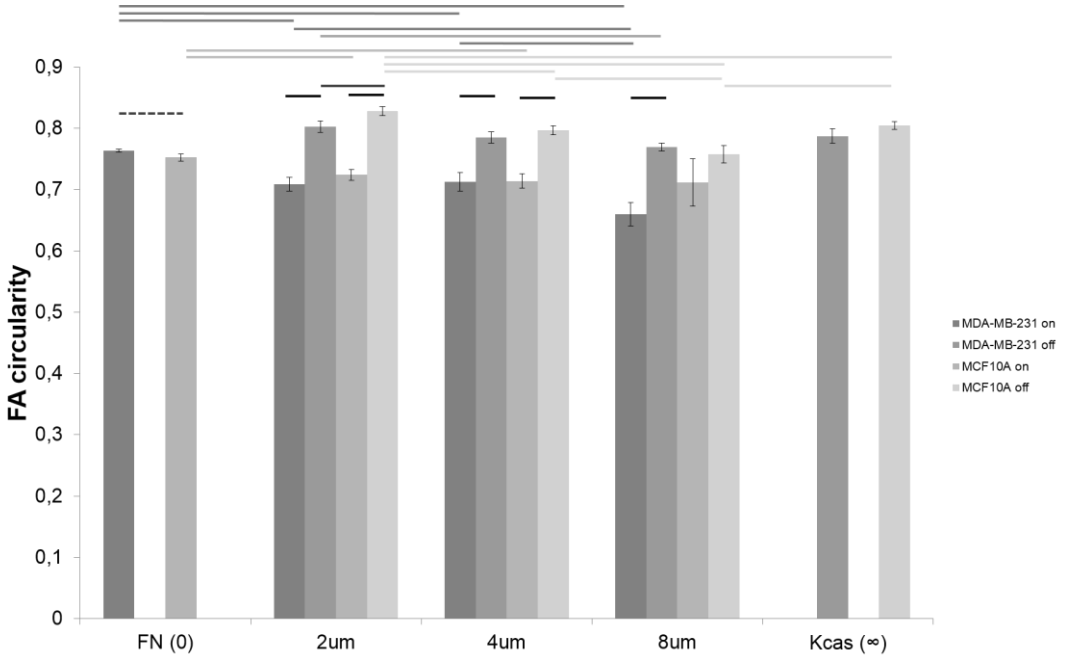

Figure 3.18. Alteration of average circularity of FAs on K-casein control, FN control and nanopattern spacings surfaces. FAs on FN nanodots are on and FAs between FN nanodots are off. FN coated surfaces have all on FAs and K-casein control surfaces have all off FAs. Horizontal solid and dashed lines show data with statistically significant differences with $p<0.05$ for two-tailed and one-tailed t-tests, respectively. (n = 9-70 cells).

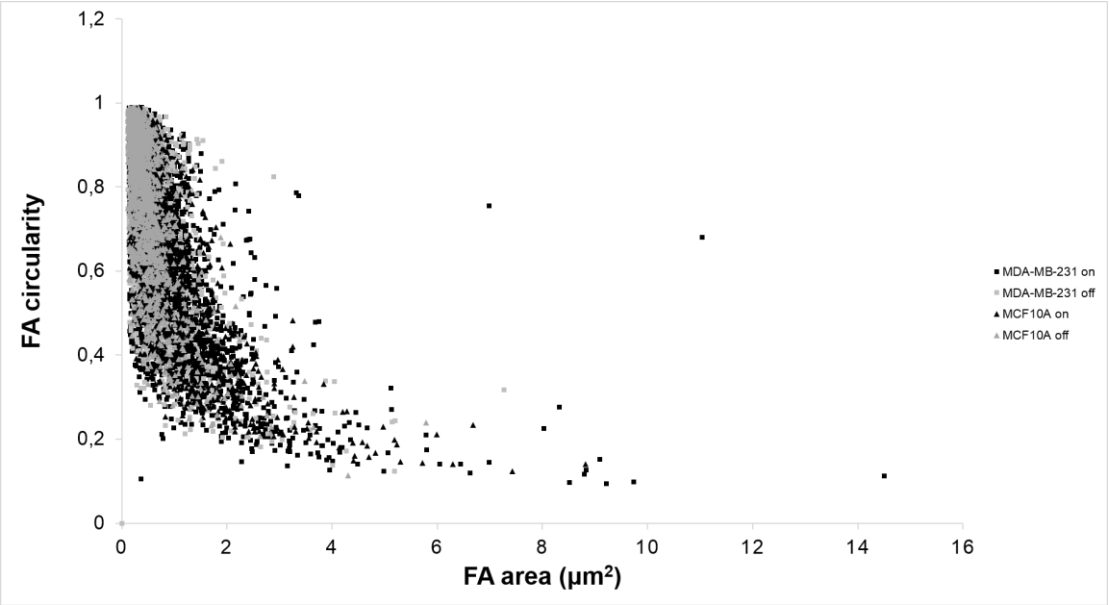

Figure 3.19. Distribution of FAs depending on individual circularities and areas on K-casein control, FN control and nanopattern spacings surfaces. FAs on FN nanodots are on and FAs between FN nanodots are off. FN coated surfaces have all on FAs and K-casein control surfaces have all off FAs.

In this study, we also tested the cells on gradiently spaced FN nanodots on K-casein coated ITO-glass surfaces. Nanodot spacing range is from 1 μm to 10 μm in one direction and other direction has constant spacings of 4 μm which is distance between lines on EBL software, so we can say that spacing range is the result of determined step size for each line. When we cultured our cells on these gradiently spacing surfaces, cells did not show any unexpected morphological variance. Immunoflorescence images of cells on gradiently patterned ITO-glass surfaces are representative regarding to morphologies (Figure 3.20). Quantitative analysis of cell morphology also supported this suggestion that cell area and cell aspect ratio reflected the similar tendencies when they were compared with 2, 4 and 8 μm spacing FN nanodots containing surfaces (Figure 3.21 and 3.22). Here, we should indicate that cells on different spacings, 1-to-10 μm, were in same data for cell morphology analysis and this made a cumulative causation for gradiently patterned surfaces. Because of this, comparison of this data with control groups which are only FN coated and only K-casein coated surfaces was more approvable. In this case, it was concluded that on the gradiently patterned surfaces, the MDA-MB-231 cells showed smaller area than FN control surface and larger area than K-casein control surfaces. As for the MCF10A cells showed similar area with FN control surface and larger area than K-casein control surface. Cell aspect ratio was similar on FN control and

patterned surfaces for MDA-MB-231 cells and smaller on K-casein control surfaces, however; MCF10A cells were more asymetric on the gradiently patterned surfaces.

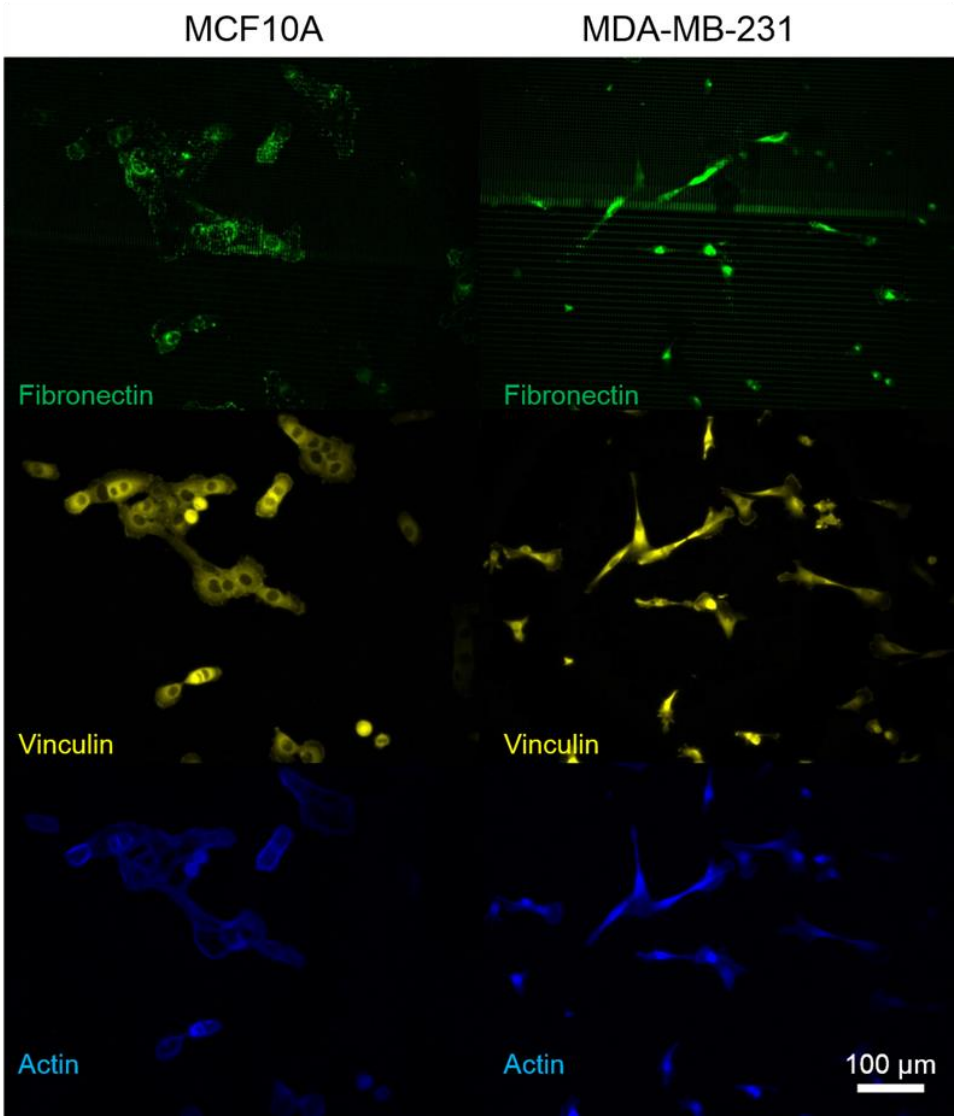

Figure 3.20. Immunofluorescence images of cells on gradiently patterned ITO-glass surfaces. Top-to-bottom, horizontal panels show fibronectin, vinculin and actin images, respectively. Left-to-right, vertical panels show MCF10A and MDA-MB-231 cells on the gradiently patterned surfaces, respectively. Scale bars show 100 µm.

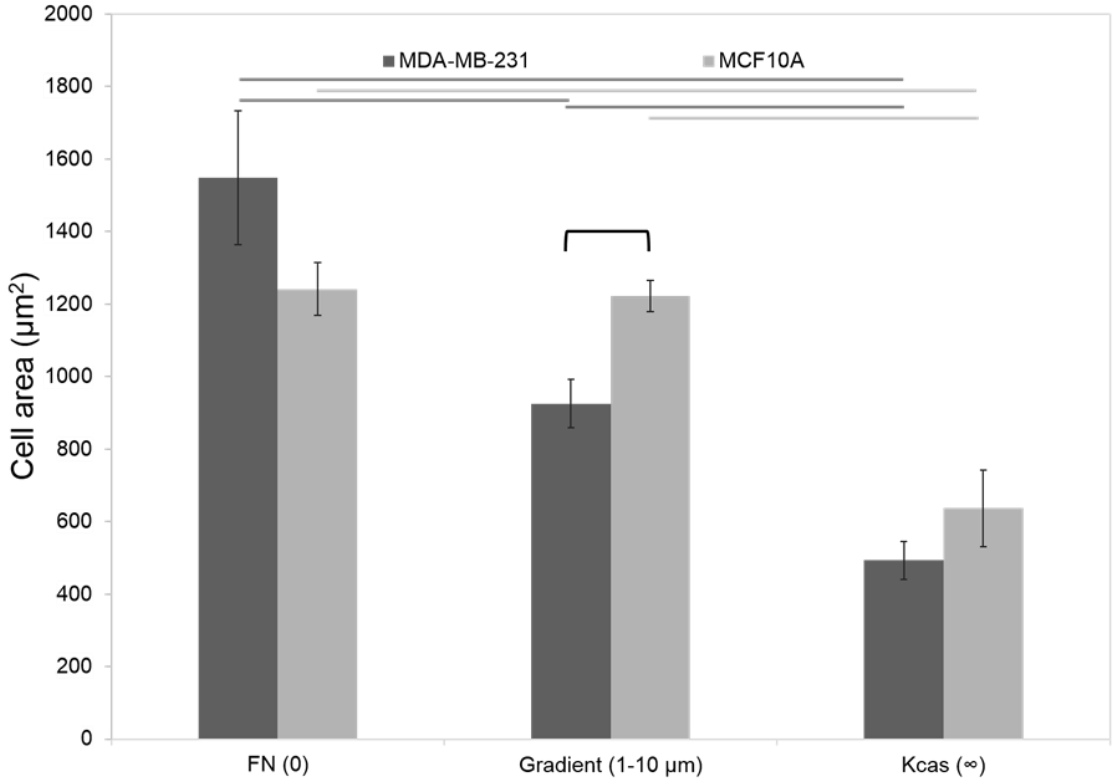

Figure 3.21. Alteration of cell area on K-casein control, FN control and nanopattern gradiently spacings surfaces. Horizontal solid and dashed lines show data with statistically significant differences with $p<0.05$ for two-tailed and one-tailed t-tests, respectively. (n = 31-70 cells).

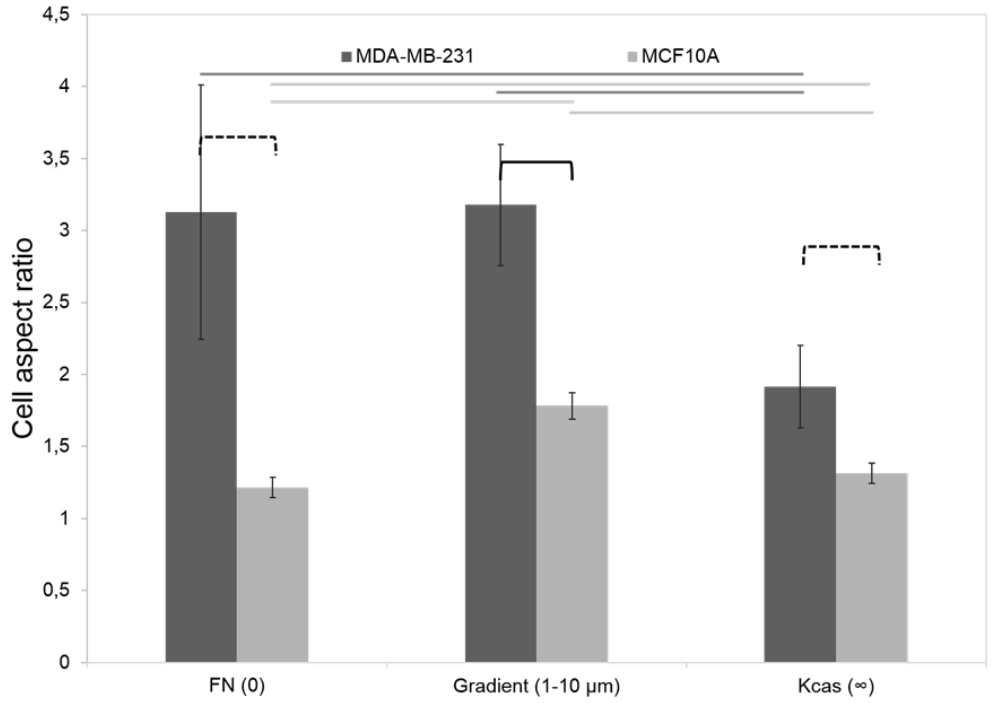

Figure 3.22. Alteration of cell aspect ratio on K-casein control, FN control and nanopattern gradiently spacings surfaces. Horizontal solid and dashed lines show data with statistically significant differences with $p<0.05$ for two-tailed and one-tailed t-tests, respectively. (n = 31-70 cells).

Gradiently patterned surfaces which consisted of differentially spacing FN nanodots (1-to-10 μm) on K-casein coated ITO-glass could also be effective for the regulation of focal adhesion and actin organization. To proof these suggestions, we analyzed the polarization tendencies of our cells on gradiently patterned surfaces. We described the measurement and calculation processes of actin polarization. FA number polarization was basically provided by coordinate-based classification. At the end of the FA quantitative analysis, ANALYZE PARTICLES command gave some other information about each particle, positional information of these FAs were enough to classify FAs according to cell center. Surface provided the directionality of polarization, increasing spacing between FN nanodots formed a stiff-to-smooth polarizable surface. Distribution of cells was largely at the smoothened regions which are close to zero at the x-axis of graphes (Figure 3.23 and 3.24). FA number polarization values were slightly above 0.5 which represents the non-polarized situations for each type of cells. Polarization value is close to 1 means positive polarization towards to the direction of decreasing spacing and value is close to 0 means negative polarization towards to the

direction of increasing spacing of FN nanodots. We expected that decreasing spacings means more FN nanodots at a defined surface should be attractive for cell adhesion. We can say that there is a slightly polarized FA formation for cells on these gradiently patterned surfaces but smooth transition was not much more effective to extremely polarize cells (Figure 3.23). Nevertheless, MDA-MB-231 cells showed their flexible behaviours when compared with MCF10A cells. In addition to FA number polarization, cells showed more notable polarizatin for their actin organization (Figure 3.24). In this case, we again say that actin polarization also reflected the difference between each cell type. As a conclusion, MDA-MB-231 cells displayed fewer interactions with FN nanodots and this made them more independent from the surface in comparison with MCF10A cells.

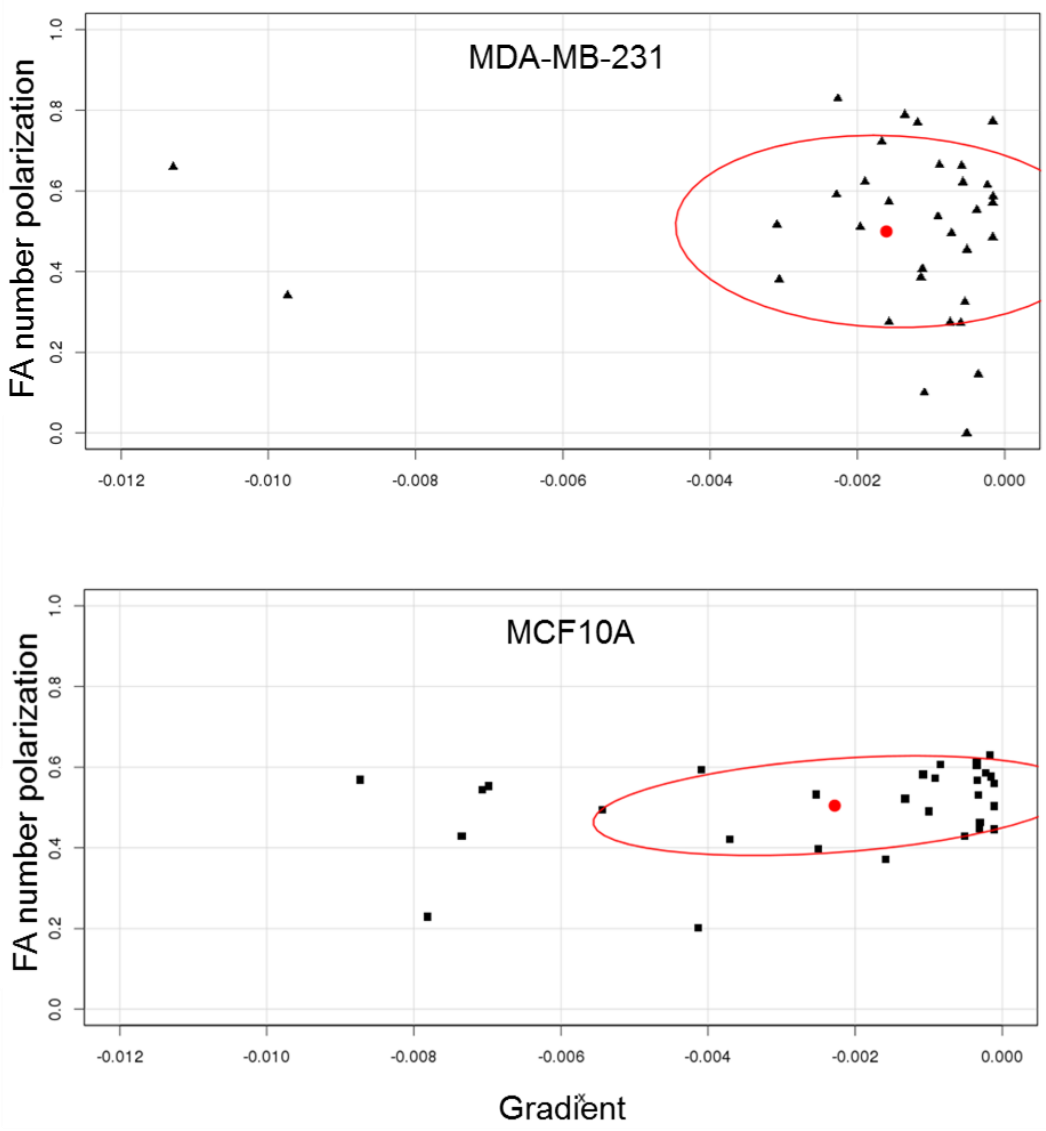

Figure 3.23. Distribution of FA number polarization versus gradient. Confidence ellipse shows 95% probability that the "true" values lie inside the region. (n = 31-34 cells).

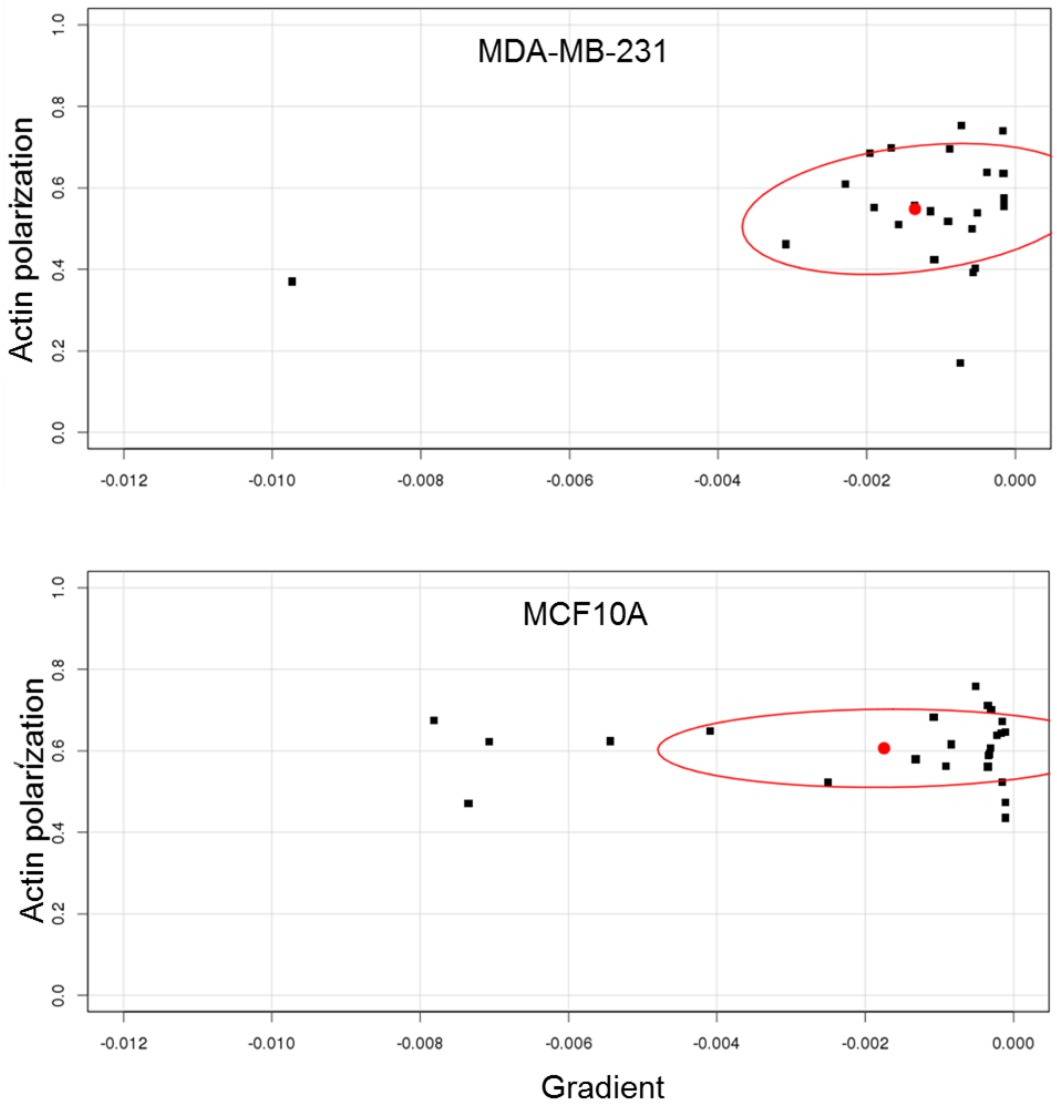

Figure 3.24. Distribution of actin polarization versus gradient. Confidence ellipse shows 95% probability that the "true" values lie inside the region. (n = 31-34 cells).

3.3. Cell Adhesion on FN Nanodots with Micrometer Spacings under Flow Conditions

Micrometer scale spacing FN nanodots on K-casein coated ITO-glasses were also tested for morphological and adhesive features of MDA-MB-231 and MCF10A cells under flow. We used patterned surfaces which were 2, 4 and 8 μm spacings between FN nanodots together with K-casein and FN control surfaces. Flow ensured a continuous shear stress over the cells. This flow-induced shear stress changed the environmental conditions in comparison with static conditions. Effects of shear stress were analyzed by means of cell area, aspect ratio and focal adhesion features. Cells did not adhere to any

surface under high shear stress which needs to high flow rate. It is known that initial tethering and rolling are essential for cell adhesion under flow, however our surfaces did not compensate these requriments in the absence of selectin molecules. Because of this, we decreased the flow rate to provide rolling on the surface by this way cells could catch initial tethering time. Integrin and fibronectin interactions are essential for activation of integrin binding, after the activation of integrin, formation of strong adhesions which are focal adhesions and quitely stronger than selectin-lectin adhesions were provided. Flow rate was 235 μl/min for shear stress 0.02 dyn/cm^2 and applied for 24 hours This shear stress was close to upper level of estimated shear stress range of interstitial shear stress. Cell adhesion was provided on the FN coated ITO-glass surfaces (Figure 3.25). We observed that when one cell adhered to the surface, another cell could adhere to surface by the help of adhered cells, so there were conglomerations on the surfaces. It was mostly seen on FN control surfaces. When we evaluated the actin images of adhered cells on FN control surfaces, we noticed organizational variations for actin cytoskeleton (Figure 3.26). These qualitative analysis showed that MDA-MB-231 cells were more divergent than MCF10A cells on account of cytoskeleton organization. While cells adhere to homogenous FN coated surfaces under flow, we did not observe any cell adhesion onto the homogenously coated K-casein surfaces. In accordance with this, adhesion to the patterned surface was also rare because surface mostly consisted of K-casein and FN nanodots occupied relatively small regions on this surface. At the end of lots of experiments, we got the adequate number of adhered cells for 2, 4 and 8 μm spacing FN nanodot containing surfaces. Under flow, cells adhered and spreaded to patterned surfaces with their focal adhesions (Figure 3.27).

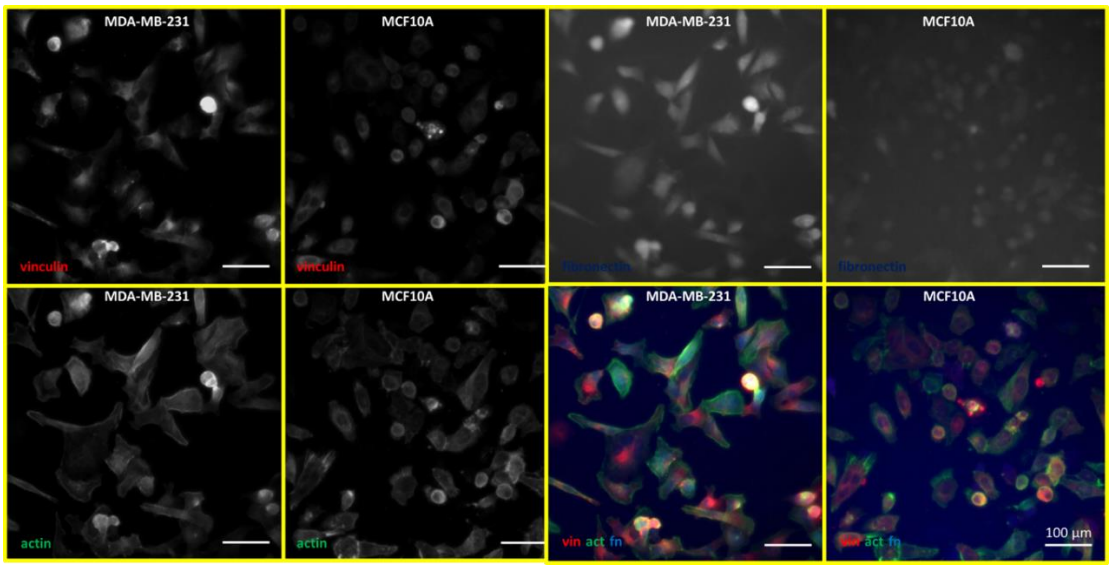

Figure 3.25. Immunofluorescence images of cells on FN coated ITO-glass surfaces after flow for 24 hours. Panels show fibronectin, actin, vinculin and merged images for MCF10A and MDA-MB-231 cells. Scale bars show 100 µm.

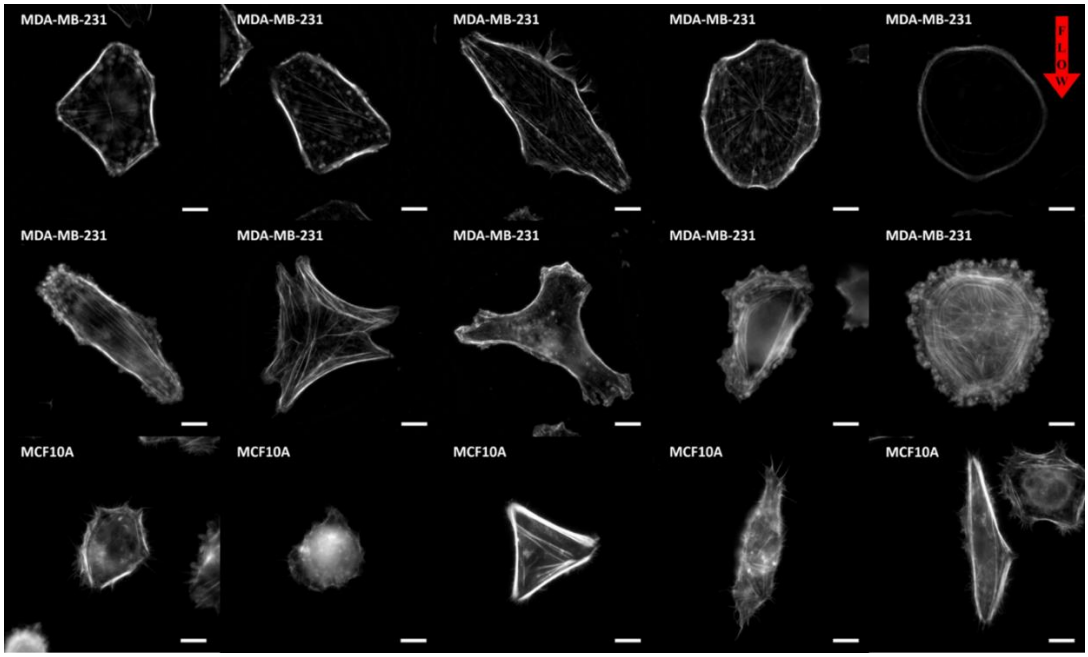

Figure 3.26. Immunofluorescence images of cells on FN coated ITO-glass surfaces after flow for 24 hours. All images show actin for MCF10A and MDA-MB-231 cells. At the top-right corner, red arrow shows the direction of flow. Scale bars show 10 µm.

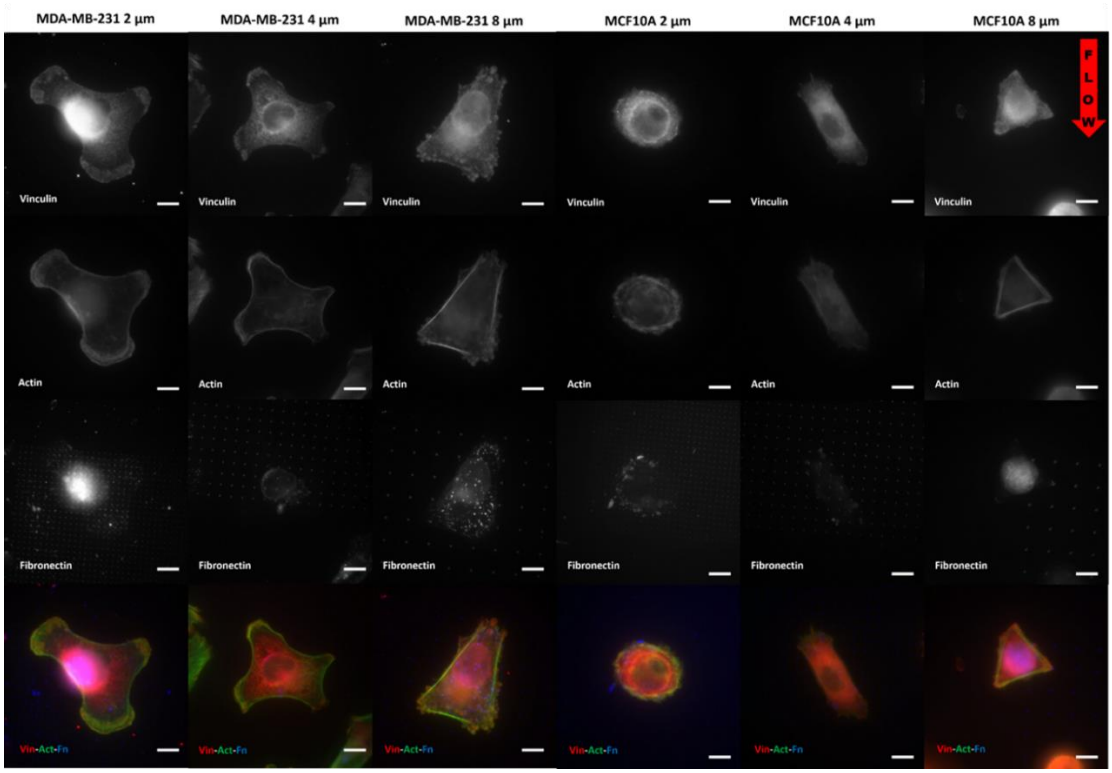

Figure 3.27. Immunofluorescence images of cells on patterned ITO-glass surfaces. Top-to-bottom, horizontal panels show vinculin, fibronectin, actin and merged images, respectively. Left-to-right, vertical panels show 2, 4 and 8 um spacings in a order of first thriple for MDA-MB-231 cells and second thriple for MCF10A cells, respectively. At the top-right corner, red arrow shows the direction of flow. Scale bars show 8 µm.

Flow conditions effected the cell morphology clearly. Cell spreaded to smaller areas and cell aspect ratio decreased in comparison with static conditions. Flow conditions also induced the difference that each cell type had more distinct differences. Areas of MDA-MB-231 cells were larger than those of MCF10A cells for FN control surfaces and patterned surfaces with 2 and 4 µm spacings (Figure 3.28). MDA-MB-231 cells were more asymmetric than MCF10A cells on fibronectin control and patterned surfaces with 2 and 8 µm spacings (Figure 3.29). In general perspective, MDA-MB-231 cells were more elongated or asymetric and they had larger areas in comparision with MCF10A cells on similar surfaces.

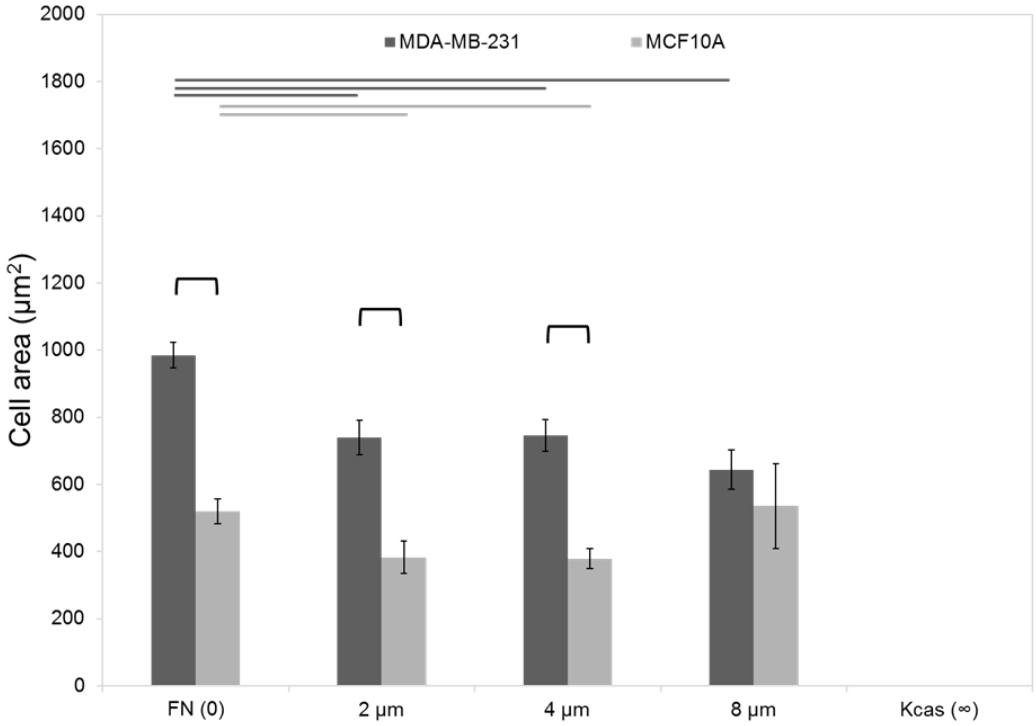

Figure 3.28. Alteration of cell area on K-casein control, FN control and nanopattern spacings surfaces under flow. Horizontal solid and dashed lines show data with statistically significant differences with $p<0.05$ for two-tailed and one-tailed t-tests, respectively. (n = 7-46 cells).

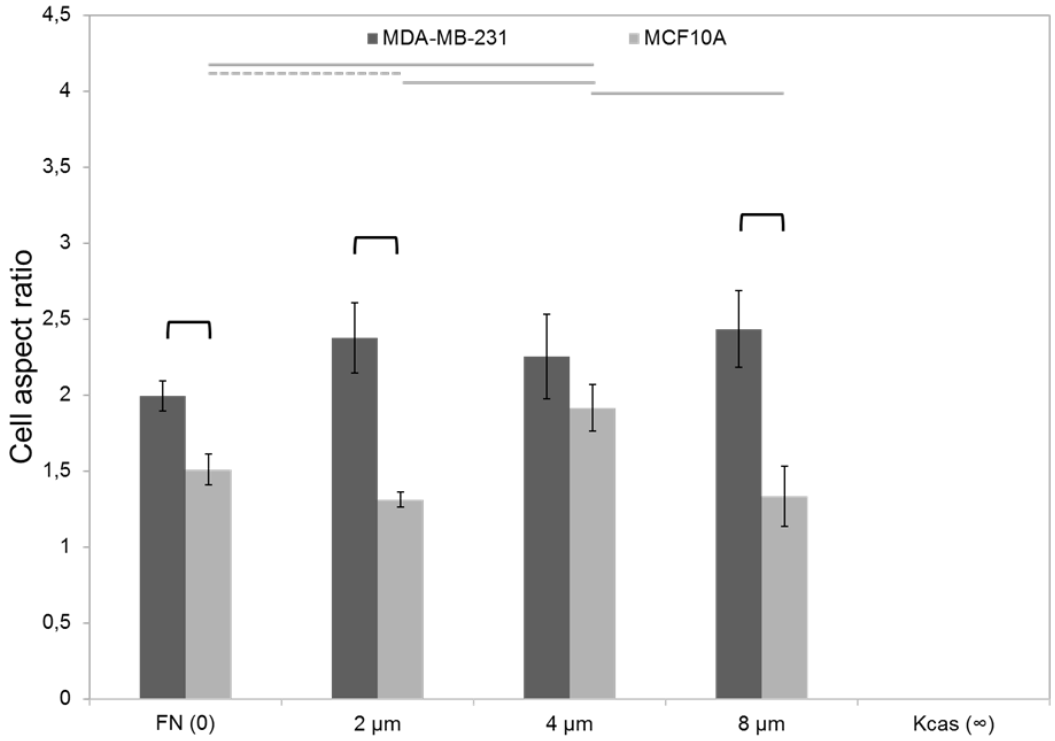

Figure 3.29. Alteration of cell aspect ratio on K-casein control, FN control and nanopattern spacings surfaces under flow. Horizontal solid and dashed lines show data with statistically significant differences with $p<0.05$ for two-tailed and one-tailed t-tests, respectively. (n = 7-46 cells).

Each cell type showed that number of FAs on FN nanodots decreased as nanopattern spacing increased (Figure 3.30). On FN control surfaces, MDA-MB-231 cells have large number of FAs with a significant difference as compared with MCF10A cells. Nanopattern surfaces with 4 and 8 µm spacings were more distinctive for cell behaviour, so cells have significant differences for on and off status with regard to FA number in itself and cells also have significant difference for their FA off numbers between each other.

Alteration of FA area is dependent to surface for each type of cells (Figure 3.31). FA area increased as nanopattern spacing increased for both cells. In this case, individual FAs enforced on more distant FN nanodots such as 8 µm. There were significant differences between FA areas of MDA-MB-231 and MCF10A cells for on and off states of 8 µm spacing.

Total FA areas decreased on FN nanodots as nanopattern spacing increased (Figure 3.32). Nanopattern surfaces with 2 µm spacings were more distinctive for cell behaviour, so cells have significant differences for on and off status with regard to total FA area between each other.

Each cell type had different circularities for their FA between on and off status (Figure 3.33). FA on FN nanodots was more linear than FAs between FN nanodots. It was clear that FAs on FN nanodots elongated and maturated with the expected interaction of integrins with fibronectins, as a result of this, FAs grew away from circular structures to more linear structures.

For distribution graph, FA area and circularity graphes was also supportive that when FAs area increased, FA circularity decreased (Figure 3.34). These data showed that maturation of FAs could be observed by increasing of their individual areas or decreasing of their individual circularities.

FA number polarization values were slightly above 0.5 which represents the non-polarized situations for each type of cells (Figure 3.35). Polarization value is close to 1 means positive polarization towards to the reverse direction of flow and value is close to 0 means negative polarization towards to the direction of flow. Cells formed slightly more focal adhesion at the reverse direction of flow for 2 μm spacing. We can say that there was a slightly polarized FA formation at the flow direction, however applied shear stress was not much more effective to extremely polarize cells. In addition to FA number polarization, cells showed more notable polarizatin for their actin organization (Figure 3.36). In this case, actin polarization of MCF10A cells was significantly distinctive at the reverse direction of flow for 4 μm spacing.

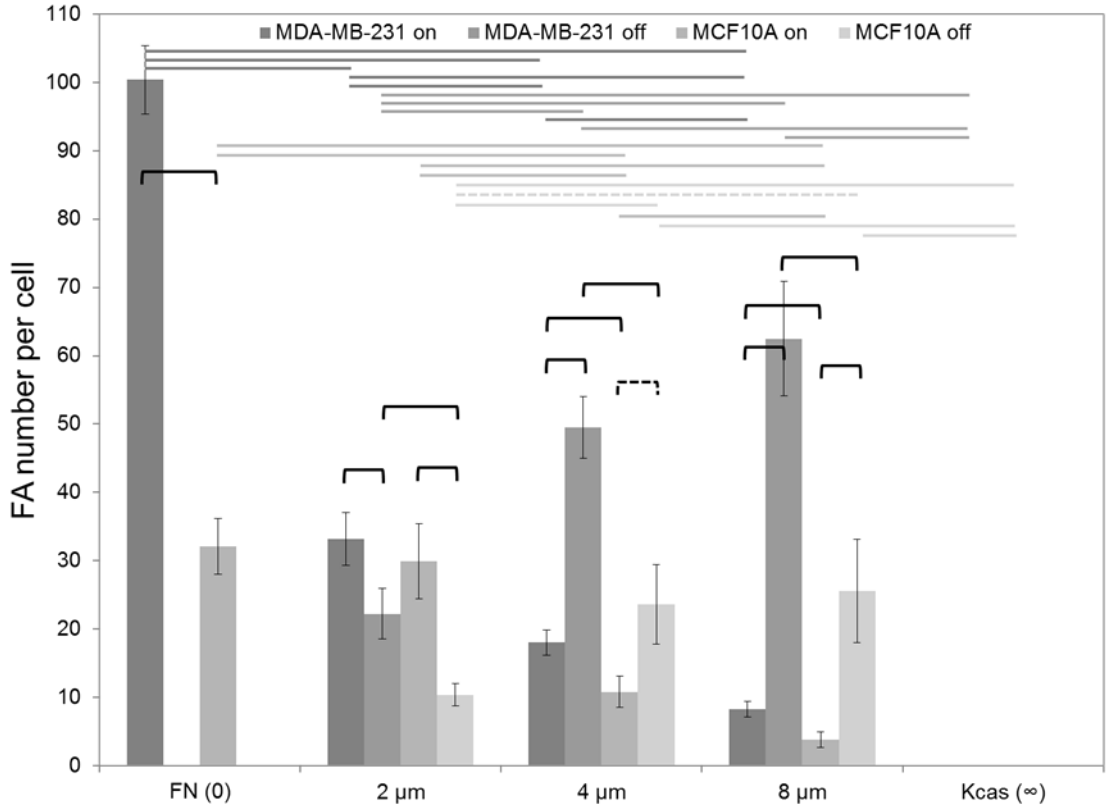

Figure 3.30. Alteration of number of FAs per cell on K-casein control, FN control and nanopattern spacings surfaces under flow. FAs on FN nanodots are on and FAs between FN nanodots are off. FN coated surfaces have all on FAs and K-casein control surfaces have all off FAs. Horizontal solid and dashed lines show data with statistically significant differences with $p<0.05$ for two-tailed and one-tailed t-tests, respectively. (n = 7-46 cells).

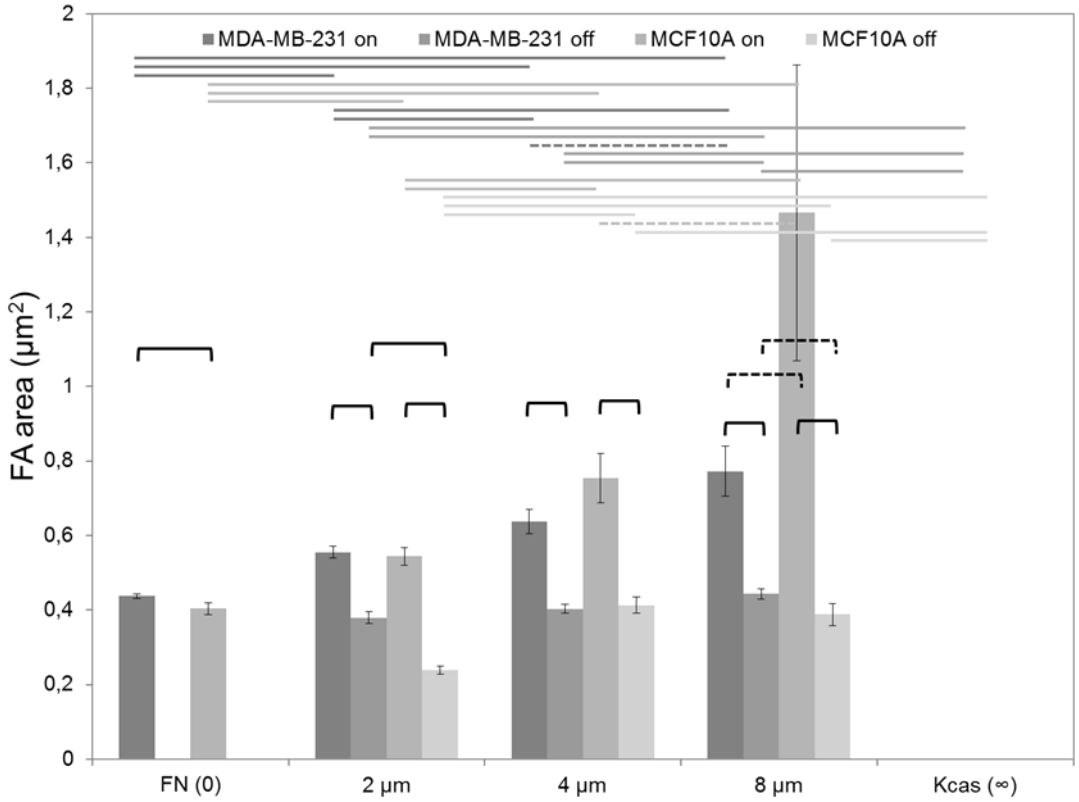

Figure 3.31. Alteration of average area of FAs on K-casein control, FN control and nanopattern spacings surfaces under flow. FAs on FN nanodots are on and FAs between FN nanodots are off. FN coated surfaces have all on FAs and K-casein control surfaces have all off FAs. Horizontal solid and dashed lines show data with statistically significant differences with $p<0.05$ for two-tailed and one-tailed t-tests, respectively. (n = 7-46 cells).

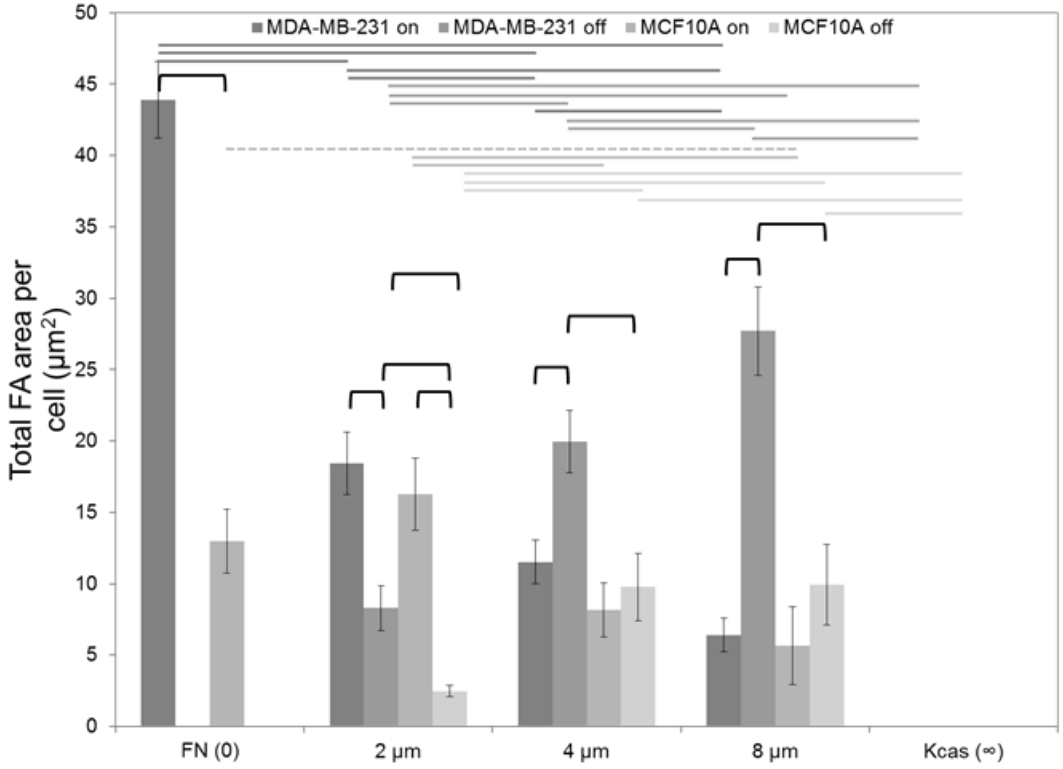

Figure 3.32. Alteration of total area of FAs per cell on K-casein control, FN control and nanopattern spacings surfaces under flow. FAs on FN nanodots are on and FAs between FN nanodots are off. FN coated surfaces have all on FAs and K-casein control surfaces have all off FAs. Horizontal solid and dashed lines show data with statistically significant differences with $p<0.05$ for two-tailed and one-tailed t-tests, respectively. (n = 7-46 cells).

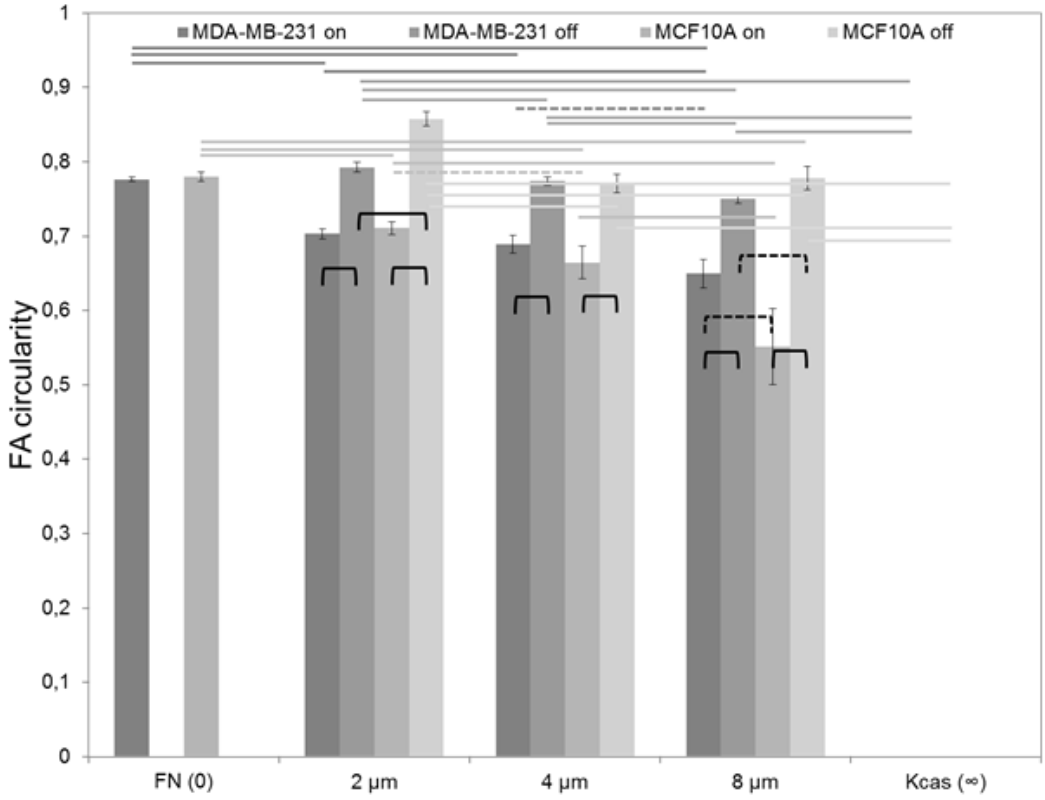

Figure 3.33. Alteration of average circularity of FAs on K-casein control, FN control and nanopattern spacings surfaces under flow. FAs on FN nanodots are on and FAs between FN nanodots are off. FN coated surfaces have all on FAs and K-casein control surfaces have all off FAs. Horizontal solid and dashed lines show data with statistically significant differences with $p<0.05$ for two-tailed and one-tailed t-tests, respectively. (n = 7-46 cells).

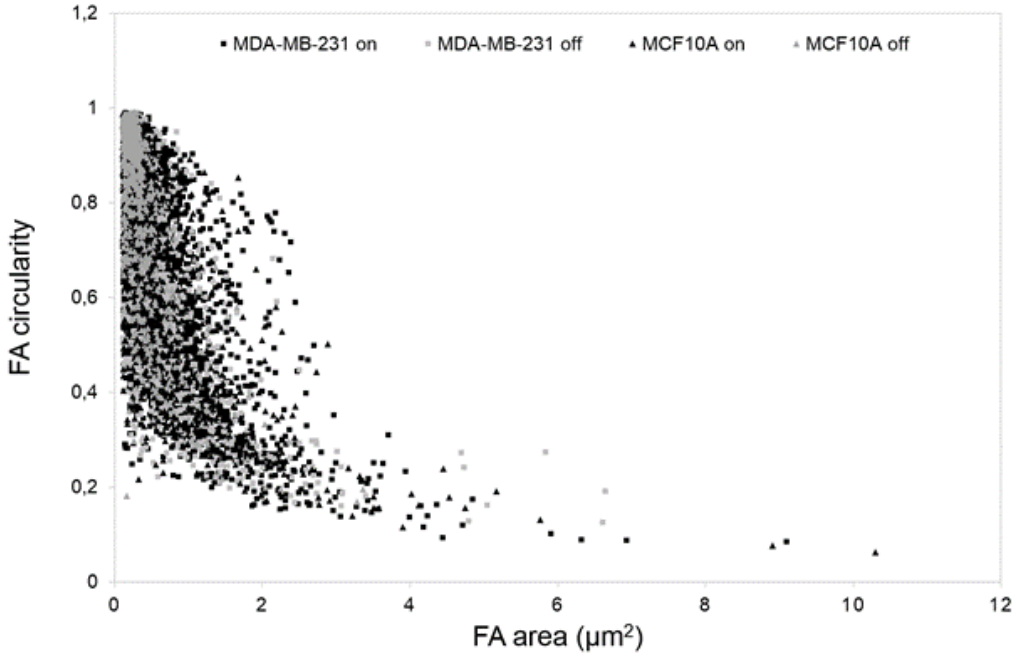

Figure 3.34. Distribution of FAs depending on individual circularities and areas on K-casein control, FN control and nanopattern spacings surfaces under flow. FAs on FN nanodots are on and FAs between FN nanodots are off. FN coated surfaces have all on FAs and K-casein control surfaces have all off FAs.

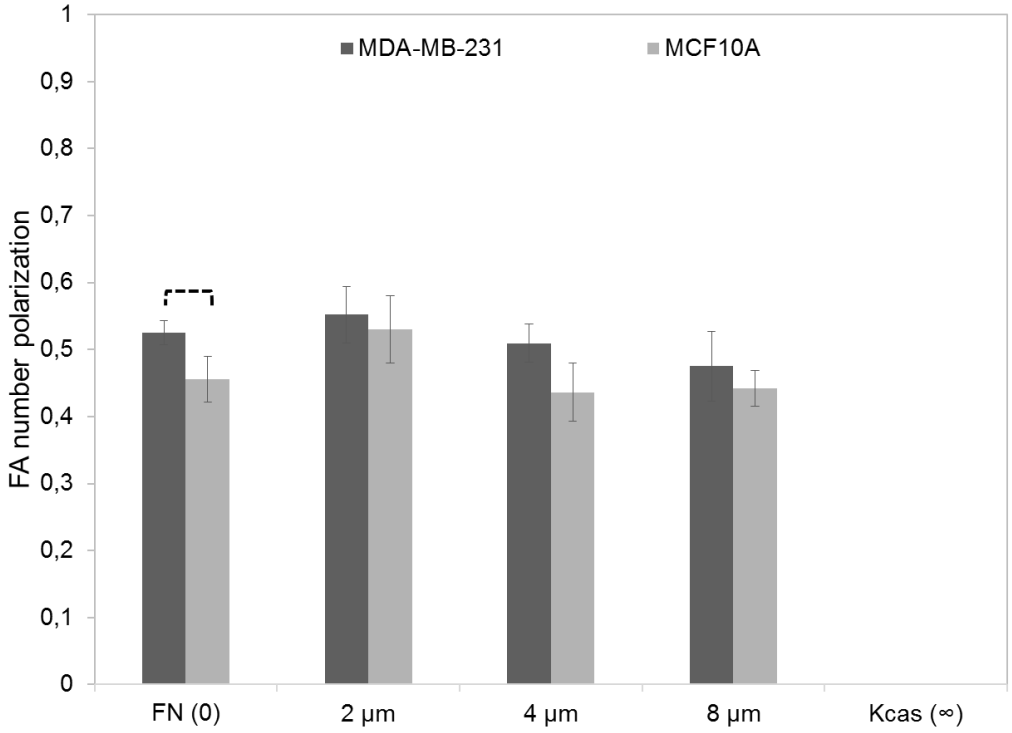

Figure 3.35. FA number polarization on K-casein control, FN control and nanopattern spacings surfaces under flow. Less than 0.5 shows negative polarization, more than 0.5 shows positive polarization, and 0.5 shows non-polarization. Horizontal solid and dashed lines show data with statistically significant differences with $p<0.05$ for two-tailed and one-tailed t-tests, respectively. (n = 7-46 cells).

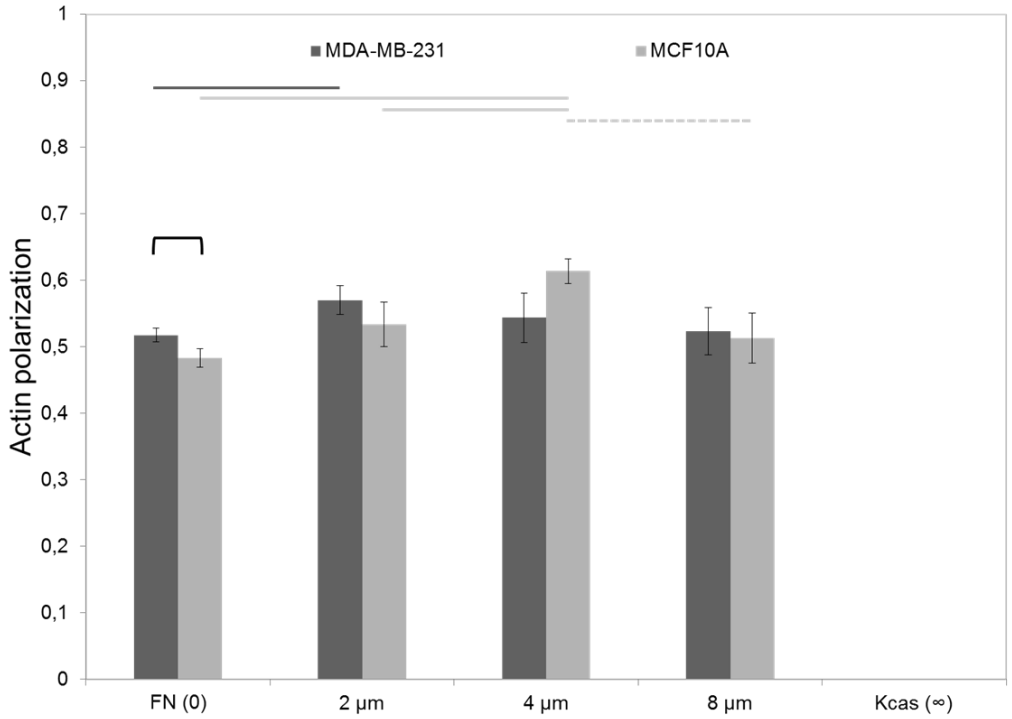

Figure 3.36. Actin polarization on K-casein control, FN control and nanopattern spacings surfaces under flow. Less than 0.5 shows negative polarization, more than 0.5 shows positive polarization, and 0.5 shows non-polarization. Horizontal solid and dashed lines show data with statistically significant differences with $p<0.05$ for two-tailed and one-tailed t-tests, respectively. (n = 7-46 cells).

CHAPTER 4

CONCLUSION

First of all, ITO-glasses were used as EBL substrates with proteins and due to a thin layer of ITO coating, ITO-glasses are transparent and thus available for many light microscopy based assays in cell biology. Functionalization of ITO-glass surfaces could be provided by APTES which induces protein binding. Protein coating of the APTES treated ITO-glasses was free of problems. Protein coated ITO-glasses were exposed to focused electron beam and backfilled with second protein without any problem. Patterned surfaces were functional at the cellular level as shown by pattern-specific focal adhesion formation. This study shows that mimicking of in vivo extracellular matrix organization could be possible on ITO-glass by direct writing on EBL. Mimicking of one of the extracellular matrix protein, fibronectin, with defined organization provided the analysis of cell morphology and focal adhesions under both static and flow conditions. Micrometer scale spacings of 2, 4 and 8 μm between fibronectin nanodots are shown to regulate cell behavior through cell morphology and cell adhesion. When the spacing between nanopatterns increase, cell area decreases under both static and flow conditions. Flow-induced shear stress is also effective on cell spreading that cell areas are relatively smaller than cells on corresponding surfaces under static conditions. Breast cancer cells can tolerate non-adhesive areas better than normal mammary epithelial cells under both static and flow conditions. Nanopatterned surfaces induce asymmetry in normal epithelial cells under both static and flow conditions. Focal adhesion features of breast cancer and normal mammary epithelial cells are differently regulated by surface protein patterns. Cells form fewer and larger focal adhesions as the spacing between nanopatterns increase under both static and flow conditions. On patterned surfaces, maturation of focal adhesions significantly occur on FN nanodots, nevertheless focal adhesions of breast cancer cells can form in a pattern-independent manner in contrast to normal mammary epithelial cells under both static and flow conditions. Overall, surfaces of 4 μm spacing was the most remarkable that these surfaces could be classified as threshold of mimicking capacity. In further studies, design and fabrication of surfaces mimicking the in vivo organization and complexity of extracellular matrix, application of the same methodology in different

fields of biological sciences and fabrication of implantable patterned surfaces can be done. Comprehensive understanding of tumor microenvironment with further studies can provide new methods for treatment of cancer. Furthermore, studies on cell migration, adhesion and extracellular matrix modifications promote evaluations of biological processes of health and disease states.

REFERENCES

Agheli, H., Malmström, J., Larsson, E. M., Textor, M., & Sutherland, D. S. (2006). Large area protein nanopatterning for biological applications. *Nano Letters*, *6*(6), 1165–71. doi:10.1021/nl060403i

Alonso, J. M., Ondarçuhu, T., & Bittner, A. M. (2013). Integration of plant viruses in electron beam lithography nanostructures. *Nanotechnology*, *24*(10), 105305. doi:10.1088/0957-4484/24/10/105305

Alsberg, E., Ph, D., Feinstein, E., Sc, B., Joy, M. P., Prentiss, M., & Ingber, D. E. (2006). Magnetically-Guided Self-Assembly of Fibrin Matrices with. *Tissue Engineering*, *12*(11).

Aumailley, M., & Smyth, N. (1998). The role of laminins in basement membrane function. *Journal of Anatomy*, *193*

Beerling, E., Ritsma, L., Vrisekoop, N., Derksen, P. W. B., & van Rheenen, J. (2011). Intravital microscopy: new insights into metastasis of tumors. *Journal of Cell Science*, *124*(Pt 3), 299–310. doi:10.1242/jcs.072728

Berginski, M. E., Vitriol, E. a, Hahn, K. M., & Gomez, S. M. (2011). High-resolution quantification of focal adhesion spatiotemporal dynamics in living cells. *PloS One*, *6*(7), e22025. doi:10.1371/journal.pone.0022025

Berrier, A. L., & Yamada, K. M. (2007). Cell – Matrix Adhesion, (June), 565–573. doi:10.1002/JCP

Biggs, M. J. P., Richards, R. G., & Dalby, M. (2010). Nanotopographical modification: a regulator of cellular function through focal adhesions. *Nanomedicine*, *6*(5), 619–633. doi:10.1016/j.nano.2010.01.009.

Blystone, S. D. (2004). Integrating an integrin: a direct route to actin. *Biochimica et Biophysica Acta*, *1692*(2-3), 47–54. doi:10.1016/j.bbamcr.2004.04.011

Boudreau, N. J., & Jones, P. L. (1999). Extracellular matrix and integrin signalling: the shape of things to come. *The Biochemical Journal*, *339 (Pt 3*, 481–8.

Cavalcanti-Adam, E. A., Volberg, T., Micoulet, A., Kessler, H., Geiger, B., & Spatz, J. P. (2007). Cell spreading and focal adhesion dynamics are regulated by spacing of integrin ligands. *Biophysical Journal*, *92*(8), 2964–74. doi:10.1529/biophysj.106.089730

Chaffer, C. L., & Weinberg, R. a. (2011). A perspective on cancer cell metastasis. *Science (New York, N.Y.)*, *331*(6024), 1559–64. doi:10.1126/science.1203543

Chang, S., Chang, C. A., Lee, D., Lee, P., Yeh, Y., Yeh, C., … Chiu, J. (2007). Tumor cell cycle arrest induced by shear stress : Roles of integrins and Smad.

Chen, C. S. (1997). Geometric Control of Cell Life and Death. *Science*, *276*(5317), 1425–1428. doi:10.1126/science.276.5317.1425

Ciobanasu, C., Faivre, B., & Le Clainche, C. (2013). Integrating actin dynamics, mechanotransduction and integrin activation: the multiple functions of actin binding proteins in focal adhesions. *European Journal of Cell Biology*, *92*(10-11), 339–48. doi:10.1016/j.ejcb.2013.10.009

Cramer, L. P., Siebert, M., & Mitchison, T. J. (1997). Identification of Novel Graded Polarity Actin Filament Bundles in Locomoting Heart Fibroblasts: Implications for the Generation of Motile Force. *The Journal of Cell Biology*, *136*(6), 1287–1305.

Danen, E. H. J., & Yamada, K. M. (2001). Fibronectin, Integrins, and Growth Control. *Journal of Cellular Physiology*, *13*(June), 1–13.

Elineni, K. K., & Gallant, N. D. (2011). Regulation of cell adhesion strength by peripheral focal adhesion distribution. *Biophysical Journal*, *101*(12), 2903–11. doi:10.1016/j.bpj.2011.11.013

Fletcher, D. a, & Mullins, R. D. (2010). Cell mechanics and the cytoskeleton. *Nature*, *463*(7280), 485–92. doi:10.1038/nature08908

Friedl, P., & Wolf, K. (2010). Plasticity of cell migration: a multiscale tuning model. *The Journal of Cell Biology*, *188*(1), 11–9. doi:10.1083/jcb.200909003

Gattazzo, F., Urciuolo, A., & Bonaldo, P. (2014). Extracellular matrix: A dynamic microenvironment for stem cell niche. *Biochimica et Biophysica Acta*, *1840*(8), 2506–2519. doi:10.1016/j.bbagen.2014.01.010

Gilcrease, M. Z. (2007). Integrin signaling in epithelial cells. *Cancer Letters*, *247*(1), 1–25. doi:10.1016/j.canlet.2006.03.031

Gill, B. J., & West, J. L. (2013). Modeling the tumor extracellular matrix: Tissue engineering tools repurposed towards new frontiers in cancer biology. *Journal of Biomechanics*, *47*(9), 1969–1978. doi:10.1016/j.jbiomech.2013.09.029

Gingras, J., Rioux, R. M., Cuvelier, D., Geisse, N. a, Lichtman, J. W., Whitesides, G. M., … Sanes, J. R. (2009). Controlling the orientation and synaptic differentiation of myotubes with micropatterned substrates. *Biophysical Journal*, *97*(10), 2771–9. doi:10.1016/j.bpj.2009.08.038

Goode, B. L., & Eck, M. J. (2007). Mechanism and function of formins in the control of actin assembly. *Annual Review of Biochemistry*, *76*, 593–627. doi:10.1146/annurev.biochem.75.103004.142647

Gutierrez, E., Petrich, B. G., Shattil, S. J., Ginsberg, M. H., Groisman, A., & Kasirer-Friede, A. (2008). Microfluidic devices for studies of shear-dependent platelet adhesion. *Lab on a Chip*, *8*(9), 1486–95. doi:10.1039/b804795b

Harjanto, D., & Zaman, M. H. (2010). Matrix mechanics and receptor-ligand interactions in cell adhesion. *Organic & Biomolecular Chemistry*, *8*(2), 299–304. doi:10.1039/b913064k

Helmke, B. P., Goldman, R. D., & Davies, P. F. (2000). Rapid Displacement of Vimentin Intermediate Filaments in Living Endothelial Cells Exposed to Flow. *Circulation Research*, *86*(7), 745–752. doi:10.1161/01.RES.86.7.745

Helmke, B. P., Thakker, D. B., Goldman, R. D., & Davies, P. F. (2001). Spatiotemporal analysis of flow-induced intermediate filament displacement in living endothelial cells. *Biophysical Journal*, *80*(1), 184–94. doi:10.1016/S0006-3495(01)76006-7

Hoa, X. D., Martin, M., Jimenez, a, Beauvais, J., Charette, P., Kirk, a, & Tabrizian, M. (2008). Fabrication and characterization of patterned immobilization of quantum dots on metallic nano-gratings. *Biosensors & Bioelectronics*, *24*(4), 976–81. doi:10.1016/j.bios.2008.07.069

Hoffman, B. D., Grashoff, C., & Schwartz, M. a. (2011). Dynamic molecular processes mediate cellular mechanotransduction. *Nature*, *475*(7356), 316–23. doi:10.1038/nature10316

Horzum, U., Ozdil, B., & Pesen-Okvur, D. (2014a). Micrometer scale spacings between fibronectin nanodots regulate cell morphology and focal adhesions. *Materials Research Express*, *1*(2), 025402. doi:10.1088/2053-1591/1/2/025402

Horzum, U., Ozdil, B., & Pesen-Okvur, D. (2014b). Step-by-step quantitative analysis of focal adhesions. *MethodsX*, *1*, 56–59. doi:10.1016/j.mex.2014.06.004

Hynes, R. O. (2002). Integrins : Bidirectional , Allosteric Signaling Machines. *Cell*, *110*(Table 1), 673–687.

Hytönen, V. P., & Wehrle-Haller, B. (2014). Protein conformation as a regulator of cell-matrix adhesion. *Physical Chemistry Chemical Physics : PCCP*, *16*(14), 6342–57. doi:10.1039/c3cp54884h

Jang, K.-J., Cho, H. S., Kang, D. H., Bae, W. G., Kwon, T.-H., & Suh, K.-Y. (2011). Fluid-shear-stress-induced translocation of aquaporin-2 and reorganization of actin cytoskeleton in renal tubular epithelial cells. *Integrative Biology : Quantitative Biosciences from Nano to Macro*, *3*(2), 134–41. doi:10.1039/c0ib00018c

Kanchanawong, P., Shtengel, G., Pasapera, A. M., Ramko, E. B., Davidson, M. W., Hess, H. F., & Waterman, C. M. (2010). Nanoscale architecture of integrin-based cell adhesions. *Nature*, *468*(7323), 580–4. doi:10.1038/nature09621

Katarina Wolf, Stephanie Alexander, Vivien Schacht, Lisa M. Coussens, Ulrich von Andrian, Jacco van Rheenen, Elena Deryugina, and P. F. (2014). Collagen-based cell migration models in vitro and in vivo. *Semin Cell Dev Biol.*, *20*(8), 931–941. doi:10.1016/j.semcdb.2009.08.005

Kim, D.-H., Provenzano, P. P., Smith, C. L., & Levchenko, A. (2012). Matrix nanotopography as a regulator of cell function. *The Journal of Cell Biology*, *197*(3), 351–60. doi:10.1083/jcb.201108062

Kou, S., Pan, L., van Noort, D., Meng, G., Wu, X., Sun, H., and Lee, I. (2011). A multishear microfluidic device for quantitative analysis of calcium dynamics in osteoblasts. *Biochemical and Biophysical Research Communications*, *408*(2), 350–5. doi:10.1016/j.bbrc.2011.04.044

Krause, M., Dent, E. W., Bear, J. E., Loureiro, J. J., & Gertler, F. B. (2003). Ena/VASP proteins: regulators of the actin cytoskeleton and cell migration. *Annual Review of Cell and Developmental Biology*, *19*, 541–64. doi:10.1146/annurev.cellbio.19.050103.103356

Lawler, K., O'Sullivan, G., Long, A., & Kenny, D. (2009). Shear stress induces internalization of E-cadherin and invasiveness in metastatic oesophageal cancer cells by a Src-dependent pathway. *Cancer Science*, *100*(6), 1082–7. doi:10.1111/j.1349-7006.2009.01160.x

Le Clainche, C., Dwivedi, S. P., Didry, D., & Carlier, M.-F. (2010). Vinculin is a dually regulated actin filament barbed end-capping and side-binding protein. *The Journal of Biological Chemistry*, *285*(30), 23420–32. doi:10.1074/jbc.M110.102830

Le Dévédec, S. E., Yan, K., de Bont, H., Ghotra, V., Truong, H., Danen, E. H., … van de Water, B. (2010). Systems microscopy approaches to understand cancer cell migration and metastasis. *Cellular and Molecular Life Sciences : CMLS*, *67*(19), 3219–40. doi:10.1007/s00018-010-0419-2

Li, J.-R., Shi, L., Deng, Z., Lo, S. H., & Liu, G. (2012). Nanostructures of Designed Geometry and Functionality Enable Regulation of Cellular Signaling Processes. *Biochemistry*, *51*(30), 5876–5893. doi:10.1021/bi200880p

Lu, H., Koo, L. Y., Wang, W. M., Lauffenburger, D. a, Griffith, L. G., & Jensen, K. F. (2004). Microfluidic shear devices for quantitative analysis of cell adhesion. *Analytical Chemistry*, *76*(18), 5257–64. doi:10.1021/ac049837t

Lussi, J. W., Michel, R., Reviakine, I., Falconnet, D., Goessl, A., Csucs, G., … Textor, M. (2004). A novel generic platform for chemical patterning of surfaces. *Progress in Surface Science*, *76*(3-5), 55–69. doi:10.1016/j.progsurf.2004.05.013

Lussi, J. W., Tang, C., Kuenzi, P.-A., Staufer, U., Csucs, G., Vörös, J., … Textor, M. (2005). Selective molecular assembly patterning at the nanoscale: a novel platform for producing protein patterns by electron-beam lithography on SiO 2 /indium tin oxide-coated glass substrates. *Nanotechnology*, *16*(9), 1781–1786. doi:10.1088/0957-4484/16/9/062

Lutz, R., Pataky, K., Gadhari, N., Marelli, M., & Brugger, J. (2011). Nano-Stenciled RGD-Gold Patterns That Inhibit Focal Contact Maturation Induce Lamellipodia Formation in Fibroblasts. *PloS One*, *6*(9). doi:10.1371/journal.pone.0025459

Malmstr, J., Lovmand, J., Kristensen, S., Sundh, M., Duch, M., & Sutherland, D. S. (2011). Different Mechanisms of Focal Adhesion Formation. *Nano Letters*, 2264–2271.

Matlin, K. S., Haus, B., & Zuk, A. (2003). Integrins in epithelial cell polarity: using antibodies to analyze adhesive function and morphogenesis. *Methods*, *30*(3), 235–246. doi:10.1016/S1046-2023(03)00030-6

Mitchell, M. J., & King, M. R. (2013). Fluid shear stress sensitizes cancer cells to receptor-mediated apoptosis via trimeric death receptors. *New Journal of Physics*, *15*(1), 015008. doi:10.1088/1367-2630/15/1/015008

Muiznieks, L. D., & Keeley, F. W. (2013). Molecular assembly and mechanical properties of the extracellular matrix: A fibrous protein perspective. *Biochimica et Biophysica Acta*, *1832*(7), 866–75. doi:10.1016/j.bbadis.2012.11.022

Natali, P. G., Botti, C., & Bigottil, A. (1992). Changes in expression of o6/P4 integrin heterodimer in primary and metastatic breast cancer. *Br. J. Cancer*, *322*(April), 318–322.

Oliva, A. A., James, C. D., Kingman, C. E., Craighead, H. G., & Banker, G. A. (2003). Patterning Axonal Guidance Molecules Using a Novel Strategy for Microcontact Printing *. *Neurochemical Research*, *28*(11), 1639–1648.

Owen, G. R., Meredith, D. O., ap Gwynn, I., & Richards, R. G. (2005). Focal adhesion quantification - a new assay of material biocompatibility? Review. *European Cells & Materials*, *9*, 85–96; discussion 85–96. Retrieved from http://www.ncbi.nlm.nih.gov/pubmed/15977138

Palankar, R., Medvedev, N., Rong, A., & Delcea, M. (2013). Fabrication of quantum dot microarrays using electron beam lithography for applications in analyte sensing and cellular dynamics. *ACS Nano*, *7*(5), 4617–28. doi:10.1021/nn401424y

Park, J., Kim, H.-N., & Kim, D.-H. (2012). Quantitative Analysis of the Combined Effect of Substrate Rigidity and Topographic Guidance on Cell Morphology. *IEEE Transactions on Nanobioscience*, *11*(1), 28–36.

Park, J., Kim, H.-N., Kim, D.-H., Levchenko, A., & Suh, K.-Y. (2012). Quantitative analysis of the combined effect of substrate rigidity and topographic guidance on cell morphology. *IEEE Transactions on Nanobioscience*, *11*(1), 28–36. doi:10.1109/TNB.2011.2165728

Parsons, J. T., Horwitz, A. R., & Schwartz, M. a. (2010). Cell adhesion: integrating cytoskeletal dynamics and cellular tension. *Nature Reviews. Molecular Cell Biology*, *11*(9), 633–43. doi:10.1038/nrm2957

Pesen, D., Erlandsson, A., Ulfendahl, M., & Haviland, D. B. (2007). Image reversal for direct electron beam patterning of protein coated surfaces. *Lab on a Chip*, *7*(11), 1603–6. doi:10.1039/b710991a

Pesen, D., & Haviland, D. B. (2009). Modulation of cell adhesion complexes by surface protein patterns. *ACS Applied Materials & Interfaces*, *1*(3), 543–8. doi:10.1021/am800264h

Pesen, D., Heinz, W. F., Werbin, J. L., Hoh, J. H., & Haviland, D. B. (2007). Electron beam patterning of fibronectin nanodots that support focal adhesion formation. *Soft Matter*, *3*(10), 1280. doi:10.1039/b710659a

Provenzano, P. P., Eliceiri, K. W., & Keely, P. J. (2009). Multiphoton microscopy and fluorescence lifetime imaging microscopy (FLIM) to monitor metastasis and the tumor microenvironment. *Clinical & Experimental Metastasis*, *26*(4), 357–70. doi:10.1007/s10585-008-9204-0

Romero, S., Le Clainche, C., Didry, D., Egile, C., Pantaloni, D., & Carlier, M.-F. (2004). Formin is a processive motor that requires profilin to accelerate actin assembly and associated ATP hydrolysis. *Cell*, *119*(3), 419–29. doi:10.1016/j.cell.2004.09.039

Ron, A., Lee, G. H., Amar, L., Ghassemi, S., & Hone, J. (2011). Adjacent assembly of self-assembled monolayers for the construction of selective bio-platforms. *Sensors and Actuators B: Chemical*, *159*(1), 75–81. doi:10.1016/j.snb.2011.06.051

Rundqvist, J., Mendoza, B., Werbin, J. L., Heinz, W. F., Lemmon, C., Romer, L. H., … Hoh, J. H. (2007). High fidelity functional patterns of an extracellular matrix protein by electron beam-based inactivation. *Journal of the American Chemical Society*, *129*(1), 59–67. doi:10.1021/ja063698a

Schwarz, U. S., Erdmann, T., & Bischofs, I. B. (2006). Focal adhesions as mechanosensors: the two-spring model. *Bio Systems*, *83*(2-3), 225–32. doi:10.1016/j.biosystems.2005.05.019

Soucy, P. a, & Romer, L. H. (2009). Endothelial cell adhesion, signaling, and morphogenesis in fibroblast-derived matrix. *Matrix Biology : Journal of the International Society for Matrix Biology*, *28*(5), 273–83. doi:10.1016/j.matbio.2009.04.005

Thievessen, I., Thompson, P. M., Berlemont, S., Plevock, K. M., Plotnikov, S. V, Zemljic-Harpf, A., … Waterman, C. M. (2013). Vinculin-actin interaction couples actin retrograde flow to focal adhesions, but is dispensable for focal adhesion growth. *The Journal of Cell Biology*, *202*(1), 163–77. doi:10.1083/jcb.201303129

Tojkander, S., Gateva, G., & Lappalainen, P. (2012). Actin stress fibers--assembly, dynamics and biological roles. *Journal of Cell Science*, *125*(Pt 8), 1855–64. doi:10.1242/jcs.098087

Tzima, E., del Pozo, M. a, Shattil, S. J., Chien, S., & Schwartz, M. a. (2001). Activation of integrins in endothelial cells by fluid shear stress mediates Rho-dependent cytoskeletal alignment. *The EMBO Journal*, *20*(17), 4639–47. doi:10.1093/emboj/20.17.4639

Van Dijk, M., Göransson, S. a, & Strömblad, S. (2013). Cell to extracellular matrix interactions and their reciprocal nature in cancer. *Experimental Cell Research*, *319*(11), 1663–1670. doi:10.1016/j.yexcr.2013.02.006

Wozniak, M. a, Modzelewska, K., Kwong, L., & Keely, P. J. (2004). Focal adhesion regulation of cell behavior. *Biochimica et Biophysica Acta*, *1692*(2-3), 103–19. doi:10.1016/j.bbamcr.2004.04.007

Zaidel-Bar, R., Cohen, M., Addadi, L., & Geiger, B. (2004). Hierarchical assembly of cell-matrix adhesion complexes. *Biochemical Society Transactions*, *32*(Pt3), 416–20. doi:10.1042/BST0320416

Zamir, E., & Geiger, B. (2001). Molecular complexity and dynamics of cell-matrix adhesions. *Journal of Cell Science*, *114*(Pt 20), 3583–90. Retrieved from http://www.ncbi.nlm.nih.gov/pubmed/11707510

Zhao, J., & Guan, J.-L. (2009). Signal transduction by focal adhesion kinase in cancer. *Cancer Metastasis Reviews*, *28*(1-2), 35–49. doi:10.1007/s10555-008-9165-4

Zhu, C., Yago, T., Lou, J., Zarnitsyna, V. I., & McEver, R. P. (2008). Mechanisms for flow-enhanced cell adhesion. *Annals of Biomedical Engineering*, *36*(4), 604–21. doi:10.1007/s10439-008-9464-5

Zoumi, A., Yeh, A., & Tromberg, B. J. (2002). Imaging cells and extracellular matrix in vivo by using second-harmonic generation and two-photon excited fluorescence. *Proceedings of the National Academy of Sciences of the United States of America*, *99*(17), 11014–9. doi:10.1073/pnas.172368799